Statistical analysis of the impact of substorms on the NMAs CPOS system in Northern Norway

Statistical analysis of the NMAs Network RTK system, where we look into the impact of substorm activity on a GNSS-receiver in Tromsø, Norway

Master student: Michael Sundøen Bitney
Supervisors: Associate Professor Lasse Clausen,
Dr. Knut Stanley Jacobsen

Thesis submitted for the degree of
Master in Physics: Space Physics
60 credits

Institute of Physics
Faculty of mathematics and natural sciences

UNIVERSITY OF OSLO

Autumn 2021

Statistical analysis of the impact of substorms on the NMAs CPOS system in Northern Norway

Statistical analysis of the NMAs Network RTK system, where we look into the impact of substorm activity on a GNSS-receiver in Tromsø, Norway

Master student: Michael Sundøen Bitney
Supervisors: Associate Professor Lasse Clausen,
Dr. Knut Stanley Jacobsen

Statistical analysis of the impact of substorms on the NMAs CPOS system in Northern Norway

`http://www.duo.uio.no/`

Printed: Reprosentralen, University of Oslo

Abstract

In this thesis we conduct a statistical analysis of the impact of substorms on NMA (Norwegian Mapping Authority) RTK Network also known as the CPOS system. A years worth of magnetometer, ROTI and GNSS position accuracy data taken from Tromsø in northern Norway is investigated. We have used the SuperMAG event list given from *Newell and Gjerloev* [2011] to find substorms and have used filtering to specify them to Northern Norway. Then we performed a superposed epoch analysis on magnetometer data, ROTI data and the GNSS accuracy.

All of the data shows a reaction at the event time and a clear correlation between the three measurements. The increase in the 95 percentile for the GNSS-noise is above the centimeter threshold that the CPOS system is suppose to deliver.

We found that substorms with low magnetometer reactions do not correlate with a decrease in GNSS accuracy, while substorms with higher magnetometer reactions do. This indicates that the substorm needs to be at a certain strength, proximity or both to have a noticeable effect on the noise level. For medium and strong substorms, the effect is present and lasts longer for the stronger substorms.

We found the filtered SuperMAG event list suitable to finding relevant substorms for northern Norway, while still having room for improvement. We found that substorms have an degrading effect on the CPOS system and is a challenge for a consistent positioning service.

Acknowledgements

I would like to express my gratitude to my supervisors Associate Professor Lasse Clausen and Dr. Knut Stanley Jacobsen. I would also like to thank Dr Anna Fæhn Follestad. They have been very helpful with my work; helping me analyze, understand the data and write about it.

I would like to thank the other master students at 4DSpace, that have helped me along the way and given me useful tips throughout the semesters. They have been very supportive throughout the two years I have worked on my master degree and made the semesters so much better. In addition I would like to thank my family with the help of housing during these difficult pandemic times, for their support and giving me a good environment to work in. I would especially thank my cat Harry for coming by when I am working and giving me a break and lower my stress.

I would also like to acknowledge the help from Kartverket with providing data from the CPOS system, which is the essential part of my thesis and would have been impossible without.

I gratefully acknowledge the SuperMAG collaborators : [1]

We acknowledge the substorm timing list identified by the Newell and Gjerloev technique *Newell and Gjerloev* [2011], the SMU and SML indices *Newell and Gjerloev* [2011]; and the SuperMAG collaboration *Gjerloev* [2012].

---

[1] `http://supermag.jhuapl.edu/info/?page=acknowledgement`

Contents

Chapter 1

Introduction

Society today is dependent on positioning systems we call GNSS (Global Navigation Satellite System). It is used for many applications, i.e. navigation in air, land and sea, in construction for property measurements and monitoring objects.

GNSS works by sending a signal from satellites to the user on the ground. By taking the time the signal takes to to get to the user and knowing the positions of the satellites, we can from this calculate the position of the user. On the way to the user, the signal needs to pass through the ionosphere. The signal can get affected by ionized plasma which causes the signal to be delayed, and this reduces the accuracy of the position. We can account for this to some degree, but during space weather events this can be difficult to fully negate.

A space weather phenomenon that can cause these disturbances, is a geomagnetic storm. A geomagnetic storm is a major disturbance to the magnetosphere. Storm activity can in extreme cases affect power grids to the point of shutting them down. It has also been known to damage satellites in orbit around the Earth and cause radiation damage to people in high altitudes such as astronauts and pilots *Buonsanto* [1999] *Eastwood* [2008], *Singh et al.* [2010]. There are also different storm events called substorms. Although they are less impactful than a full geomagnetic storm, they are much more frequent and are mainly of interest at high latitudes. Both of these events are a problem to the GNSS-system and can in some cases knock out standard GNSS-receivers completely. In many cases, these substorms can make the GNSS-receiver inaccurate with an error up to several meters. The usage of GNSS receivers in high latitudes is growing *Moen et al.* [2013], showing that there is a need for further studies.

One major improvement in recent decades is the Network RTK (Real Time Kinetic) GNSS-receivers, which provide corrections of common error i.e. ionospheric error. These corrections are given within a second using base stations close to the user's GNSS-receiver. These base stations provide measurements using dual frequency GNSS-receiver and help the user's GNSS-receiver solve the position better. Norway uses the CPOS (Centimeter POSitioning)-system from the NMA (Norwegian Mapping Authority) that provides this system. Despite being very accurate, there is a need to further study the impact of substorms on the Network RTK GNSS-receivers to see how they behave. This is due to the CPOS system has been shown to be vulnerable to space weather *K.S. Jacobsen* [2012].

In this thesis, we investigate the effect substorms have on the CPOS system in Northern Norway. We looked at the year of 2018 and found times for possible substorm event times from the SuperMAG event list given in *Newell and Gjerloev* [2011]. This provides us with a number of possible events for 2018 globally, but we will use filtering to make the list relevant for Northern Norway specifically. We have investigated this list using 3 different data sources. We used the Tromsø magnetometer to look for increases in auroral electrojet as this is a typical indicator of a substorm activity *Gjerloev et al.* [2004]. This is to see what sort of change we see during the events and to validate the filtered lists relevance to Northern Norway.

We looked into ROTI data at Tromsø, which measures the changes in ionospheric plasma as this has been a good indicator of disturbances of the GNSS *Jacobsen and Dähnn* [2014]. To look into direct impacts of the CPOS system, we have analyzed data from a fixed GNSS-receiver that uses CPOS in Tromsø to determine the accuracy of the positioning. Then we perform a superposed epoch analysis on the data and look at how a typical substorm behaves and how this affect GNSS positioning that uses the CPOS system.

In this thesis, we will start to go through the relevant theory for understanding space weather and GNSS is presented. The Methods section explains how the data was prepared for analysis. In the Result section, the processed SuperMAG event list and the superposed epoch analysis are presented. Finally, the results will be discussed and conclusions will be presented, and suggestions for future work are given.

Chapter 2

Theory

This is an introduction to the theoretical background of space weather and GNSS (Global Navigation Satellite System).

2.1 The Solar Winds

The Sun is a star in the center of our solar system and is essential for life on Earth. It has a mass of 1.99 $\cdot 10^{30}$ kg and consists of plasma at a very high temperature. The Sun's outer atmosphere has strong magnetic fields, which follow a 11 year cycle, where it goes from a lower level to higher level of solar activity. This can be seen from the number of sunspots on the Sun, where a sunspot is a dark region which typically indicates powerful magnetic field lines. A low sunspot number relates to low activity on the Sun and a high sunspot number relates to high activity. This also relates to the amount of plasma ejected from the Sun. The plasma emitted creates high-energy solar winds in the interplanetary space. The magnetic field in the solar wind and the interplanetary medium is called the IMF (Interplanetary Magnetic Field).

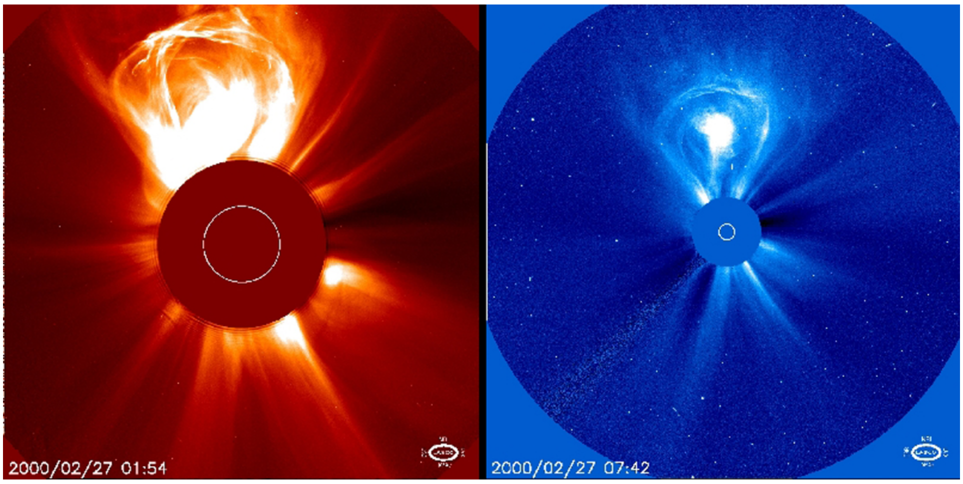

Figure 2.1: Here we have a picture of the Sun where a CME (Coronal Mass Ejection) occurs on February 27 2000. The CME can be seen in both pictures as an arc that flings plasma into space. This can cause a major increase in the speed, mass and temperature of the solar wind, which have a big impact on Earth. Credit: SOHO ESA & NASA

At times, plasma can escape the Sun in violent eruptions which are called CMEs (Coronal Mass Ejections) *Hundhausen* [1999], as seen in Figure 2.1. This can greatly increase the amount of plasma contained in the solar wind. As the solar wind moves, the magnetic field can be considered to be frozen in to the plasma and moves with it. This is called the frozen in theorem *Owens and Forsyth* [2013] and the plasma can be considered a fluid. We can make measurements of the solar wind, i.e temperature, magnetic field strength, magnetic field direction and flow speed. These measurements are important as the solar wind will reach Earth and interact with the Earths magnetic field.

2.2 Magnetosphere

The magnetosphere is the area of space around the Earth where the Earth's magnetic field is contained. This magnetic field is vital for life on Earth as it shields us from the solar wind. An illustration of the magnetic field can be seen in Figure 2.2. The magnetic field has the approximate shape of a dipole magnet, but with the effect of the solar wind, it has a slightly more comet like shape with a tail facing away from the Sun. We will use two terms to describe magnetic field lines. Ones is open magnetic field lines which go into space and are located at high latitudes at the north and south magnetic poles. The other is closed magnetic field lines, however, which return to Earth and are the inner magnetic lines in the lower latitudes.

At the north and south polea, there are open magnetic field lines. We call the boundary between the closed and open magnetic field lines the OCB (Open Closed field line Boundary). We will call the side of the Earth that faces the Sun dayside and the other side nightside.

As the solar wind hits the Earth, it gets deflected and decelerated by the bow shock as the solar wind encounters the magnetic field of the earth. The bow shock is usually about 8-12 Earth radii (R_E) on the dayside of the Earth. Closer towards Earth, we have a point where the pressure from the Earth's magnetic field matches the solar wind pressure and that is the magnetopause. It moves around the dayside and extends into space on the nightside.

The magnetosheath is the area between the bow shock and the magnetopause where high magnetic turbulence and complex currents can be found *C.T. Russel and Strangeway* [2016], *Pécseli* [2013a]. The magnetotail is the magnetic field lines on the nightside which extends into space and can be more than 200 R_E long *Campbell* [2003]. These parts of the magnetosphere can be seen in Figure 2.2. For further reading about the magnetosphere, see chapter 10 in *C.T. Russel and Strangeway* [2016].

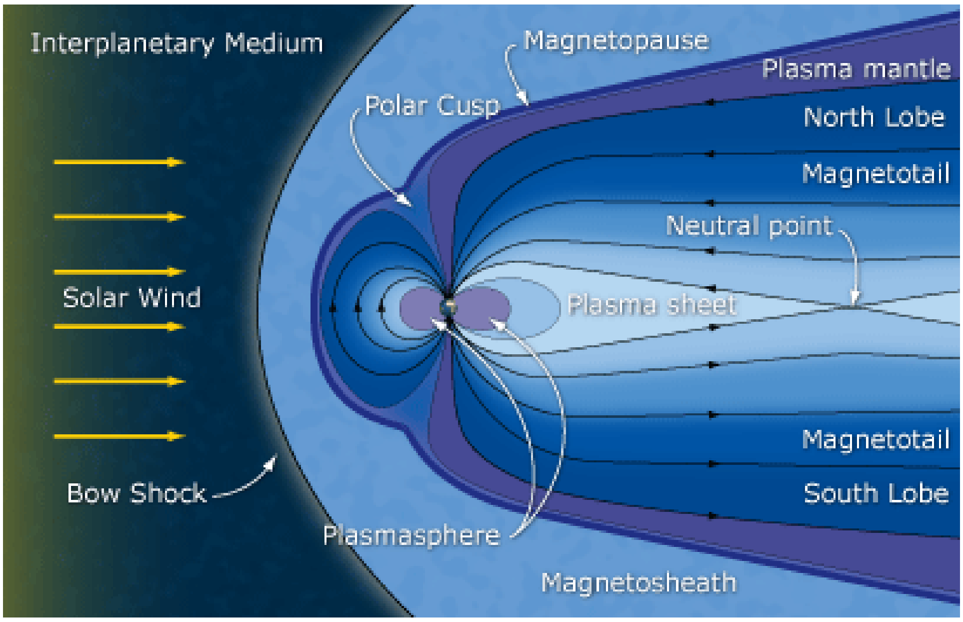

Figure 2.2: The Figure illustrates the structure of the Earth's magnetosphere and its interaction with the solar wind. Here the dayside is on the left on the side of the solar wind and the nightside is on right. In addition, it shows the solar wind, bow shock, magnetosheath, magnetopause, magnetotail and plasmapshere.The Figure is from *ESA* [2007]

a Dungey cycle

A vital process of the interaction of the solar wind with the magnetosphere is the Dungey cycle. The Dungey cycle describes the process when the solar wind interacts with the Earth's magnetic field and it was first described in *Dungey* [1961]. It describes how the solar wind can deposit energy and plasma into the magnetosphere *Paschmann et al.* [1979].

To visualize this cycle, we will describe the different field lines shown in Figure 2.3. The upper drawing shows the Dungey cycle from a solar wind interactions perspective, while the lower drawing shows the movement of plasma at the ionospheric footprint of the magnetospheric magnetic field line. We will call the area where the open field lines extends out to space on Earth for the polar cap.

Line 1 is the reconnection on the dayside. Reconnection is a merge between two magnetic fields *Yamada et al.* [2010]. In order for this to happen, we need the magnetic field of the solar wind to point southward. This means the magnetic field direction of the solar wind is the opposite direction of the Earths magnetic field. This leads to a reconnection turning closed magnetic field lines of the Earth to become open magnetic field lines that completes with the solar wind. This allows energy and plasma to pass through to the magnetosphere and travel to the ionosphere. We will explain the ionosphere in a later section.

As the magnetic field lines are opened, they move with the solar wind towards the night side, which is illustrated by lines 2 and 3.

A segment that is not highlighted in the upper drawing in Figure 2.2 is the OCB (Open Closed magnetic field line Boundary). The OCB is where the magnetic field lines go from closing lines that complete on Earth to open lines which go into space *Clausen et al.* [2013]. This can be seen in the lower drawing of the magnetic pole in Figure 2.3. In lower part of the Figure, the numbers correlate to the upper part of the Figure and show how the magnetic field lines move through the middle of the polar cap as the Dungey cycle progresses. As we move towards line 5, the open magnetic field lines will start to close on the nightside. This can add magnetic flux to the magnetotail and can cause a reconnection to occur on the nightside. If a reconnection occurs, the plasma and energy that is stored in the tail will follow the closed field lines towards the magnetic poles, which is illustrated by lines 6 and 7. The open magnetic field line will be closed and will move towards the dayside as seen in lines 8 and 9 in the lower drawing in Figure 2.3.

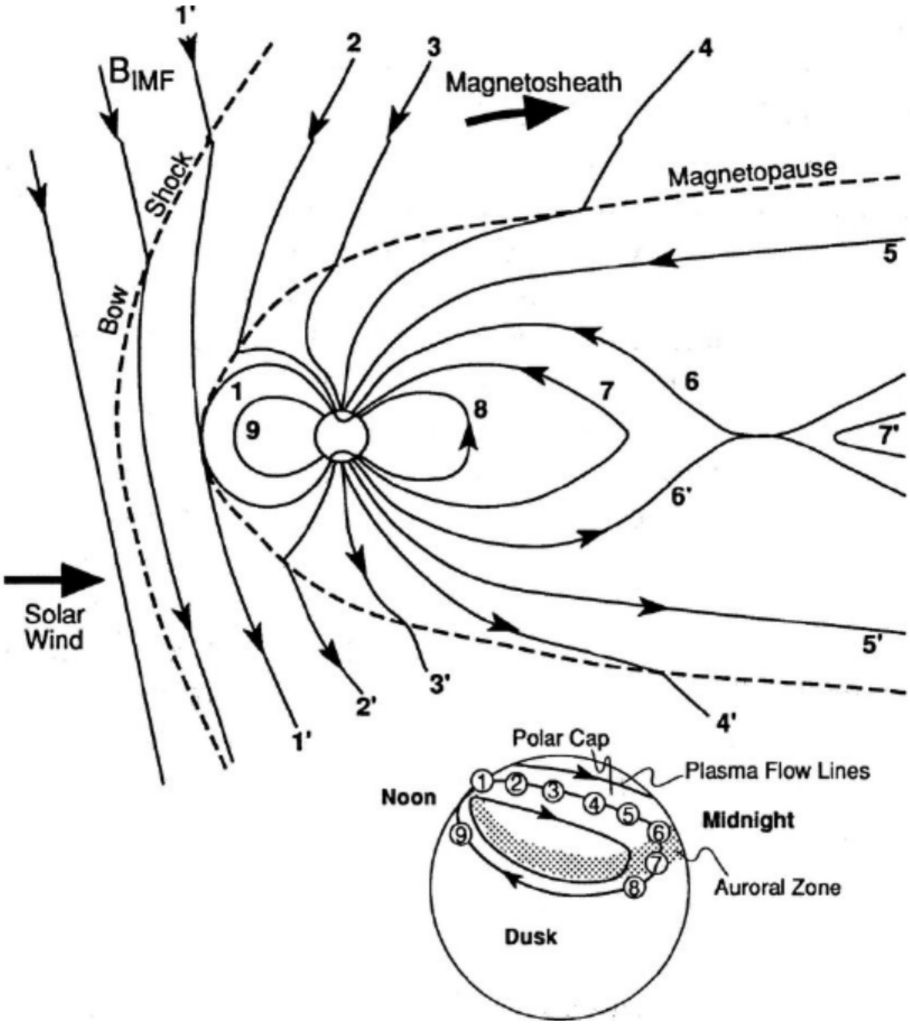

Figure 2.3: This figure shows how the Dungey cycle occurs. The upper drawing shows the Dungey cycle from a solar wind interactions perspective, while the lower drawing shows how the Dungey cycle behaves from a polar cap perspective. Note that we can have reconnection at two places; the dayside, where the magnetopause meet the solar wind above the equator and on the nightside at line 6 in the upper drawing. The figure is from the book *C.T. Russel and Strangeway* [2016]

It is also interesting that the OCB on Earth, also called the polar cap boundary, moves depending on solar wind conditions and can be explained by the ECPC paradigm *Cowley and Lockwood* [1992], *Siscoe and Huang* [1985]. If we have a dayside reconnection, the polar cap boundary will expand equatorward and if we have a nightside reconnection, the polar cap boundary will contract toward the magnetic pole.

2.3 Storm activity; Storms and substorms

A geomagnetic storm is a major disturbance of the magnetosphere caused by the solar wind interactions *Gonzalez et al.* [1994]. They can last for many hours or several days and are a global phenomenon. We can detect and measure a geomagnetic storm using DST (Disturb Storm Time) index, which measures the ring current. Using the DST, the geomagnetic storms can be ranked as moderate (50-100 nT), intense (100-250 nT) and super-storms (>250 nT) *Cander and Mihajlovic* [1998]. Extreme storms over 400 nT are rare, but do happen *Gonzalez et al.* [2011].

A substorm is also considered a disturbance of the magnetosphere, but this occurs more independently from the solar wind and occur when the magnetosphere system releases energy. It is smaller than a geomagnetic storm, but substorms occur more frequently. Substorms are more of a local phenomenon which can cause effects such as aurora at the auroral oval *Rostoker et al.* [1980]. Aurora is sometimes difficult to see due to cloudy weather or midnight Sun during the summer and therefore are not a reliable way to detect substorms. A substorm will typically last an hour and can occur multiple times over a night. They can be triggered by a geomagnetic storm.

In both a substorm and a storm, the plasma will travel in the OCB to the auroral oval and will be visible as the Polar light, Aurora Borealis. One can identify the location of the OCB by looking at the location of the Aurora Borealis in satellite imaging *Germany et al.* [1997], *Frank and Craven* [1988]. One can also see the effect of substorms by looking at currents in the ionosphere.

2.4 Ionosphere

The ionosphere is a partially ionized region of the atmosphere. Together with the magnetosphere, it plays an important part in shielding the Earth from radiation and plasma from the Sun. The ionosphere absorbs UV-rays and X-rays from the Sun, which creates ionized plasma and is called photoionization. This produces most of the plasma, especially at the equator as there is more sunlight. In high latitudes, we have particle precipitation which are energetic particles from the magnetosphere *Prölss* [2012].

TEC (Total Electron Content) is a measurement of how much plasma there is in an area. The definition is shown in equation 2.1. The unit for TEC is TECU (Total Electron Content Unit) and is defined as 10^{16} electrons/m^2.

$$\text{TEC} = \int_S n_e \, dS \tag{2.1}$$

When the ionosphere is disturbed by an event like geomagnetic substorm activity, it creates convection of the plasma and can set up powerful currents. During substorms, plasma flows from the magnetotail and we get particle precipitation. The energized particles entering the ionosphere will add to the amount of plasma and therefore increase the TEC measured significantly. This is both visible as Aurora Borealis and will increase the strength of currents like the auroral electrojet and field aligned currents also known as Birkeland currents *Kamide and Akasofu* [1976]. The auroral electrojet is typically found around high latitudes. As in electrical circuits, the currents can not just go from A to B, but need to be fully closed as a circuit. The auroral electrojet moves westward and the FAC (Field Aligned Currents) will then move into space aligning with the magnetic field. Thereafter, the FAC will move to the south pole, where it connects with equivalent auroral electrojet that moves eastward. From there, it goes up into space again and reconnects with northern auroral electrojet completing the circuit *Wang et al.* [2005]. This is illustrated in Figure 2.4.

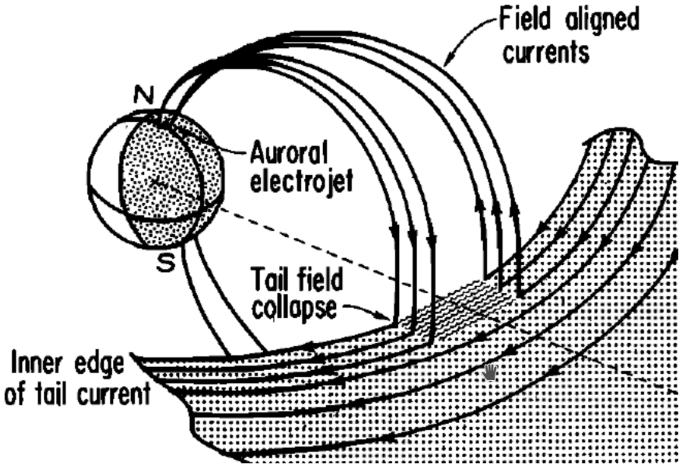

Figure 2.4: Here we see the auroral electrojet on Earth moving westward on the northern hemisphere. This current is completed by the Birkeland current FAC (Field Aligned Current) which move aligned with the magnetic field line into the magnetosphere. The FAC will move toward the south, where there is a Auroral electrojet moving in the opposite direction. From there, another FAC will complete the circuit as it move to the north again. Figure is copied from *McPherron et al.* [1973]

The Auroral electrojet and other currents in the ionosphere are of interest, due to Biot-Savarts law, equation 2.2, which says that a current will set up a magnetic field. We can detect these currents from the ground using a magnetometer, which is a device that can measure magnetic fields.

$$\vec{B} = \frac{\mu_0}{2\pi} \int_C \frac{I\, d\vec{l} \times \hat{r}}{|\vec{r}|^2}. \tag{2.2}$$

In equation 2.2, the $\vec{B}$ is the magnetic field, μ_0 is the permeability of the medium, I is the current and the integral is a line integral over path C where the currents flows. Note that that we divide by r^2, so the further away we are from the current, the weaker the magnetic field. We can see an illustration of this in Figure 2.5, where the magnetometer can detect the magnetic field that is created by the current.

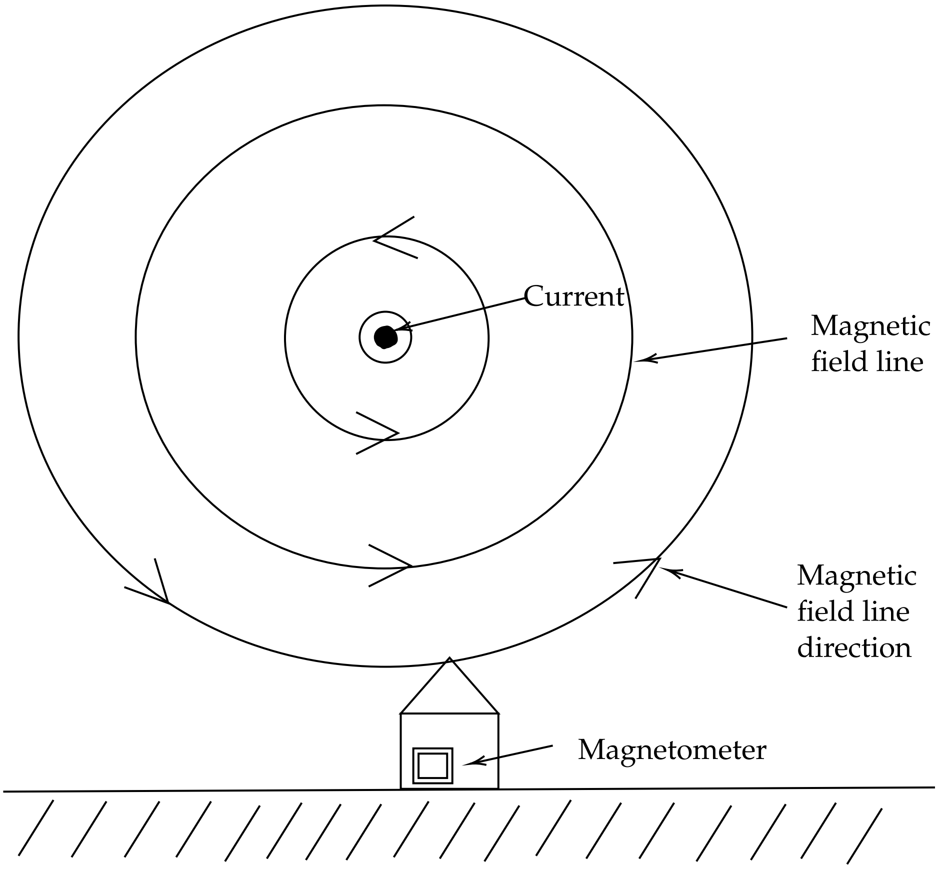

Figure 2.5: Here we have an illustration of how a current generated by the plasma moving in the ionosphere has a widespread magnetic field as Biot-Savarts law 2.2. The current moves out of the page and the right hand rule is used to find the direction of the magnetic field. This makes it possible to detect currents on ground, as one can measure changes in the magnetic field as an indication that there is a current being created in the ionosphere.

The auroral electrojet is of interest, as it is used as an indicator of substorm behavior *Gjerloev et al.* [2004]. However, the auroral electrojet is not always at the same latitude as it moves with the expansion and contraction of the polar cap. To measure the auroral electrojet, we can use the AE (Auroral Electrojet) index *Davis and Sugiura* [1966b]. This uses magnetometers from 10-13 observatories along the auroral zone and there we look for the highest value, AU (Auroral Upper) and the lowest value, AL (Auroral Lower) of the magnetometer stations. Note that this is the H-component of the measurement. Here H = $\sqrt{x^2 + y^2}$ of x,y,z coordinate system. The AE index is then derived by the following equation AE = AU - AL.

2.5 GNSS (Global Navigation Satellite Systems)

Here we go through the basics of how a GNSS receiver works. A lot of this information is taken from the book *Hofmann-Wellenhof* [2008]

A GNSS-receiver works by receiving signals from artificial satellites and then calculates the time the signal uses from the satellites to the receiver to calculate the position. The signal sent is between 1-2 GHz and contains the information needed, i.e. orbit information and the time the signal was sent. The most known systems are the American GPS, the European Galileo, the Russian GLONASS and the Chinese BeiDou. These satellites are located in MEO (Medium Earth Orbit).

Unfortunately, the measured distance between the satellite and the GNSS-receiver is not completely accurate. We need to account for the errors from various sources. Therefore, we call the calculated distance from the satellite to the receiver pseudorange.

a Pseudorange

Pseudorange R is the calculated distance, which includes various delays and ρ which is the geometric distance. This is represented in equation 2.3.

$$R = \rho + c\delta \tag{2.3}$$

Here we get a time delay δ, which causes a different distance to be calculated than the actual length. Since c, the speed of light is a very high velocity, a small delay can have a large effect on the positioning. As an example, a delay by 3.33 nanoseconds can produce a meter offset from the actual position. So in order to get accurate positioning, a detailed understanding of the causes of the time delays is needed to reduce error as much as possible.

This time delay δ is a combination of many effects and can be seen in equation 2.4. You can see a visualization of these errors in Figure 2.4.

$$R = \rho + c(dt_r - dt^s) + T + \alpha_f \mathrm{STEC} + K_{P,r} - K_P^s + \mathcal{M}_P + \epsilon_P \tag{2.4}$$

Here dt^s is the time error in the satellite clock and dt_r is the time error in the receiver clock. Although these clocks are accurate, they are not fully synchronized. This will affect the timing of the signal and can cause an error.

The clock error in the satellite is lower compared to the receiver clock, since the satellite has a more accurate atomic clock. However, one can calculate the error by solving the position with a fourth unknown; clock error. This means you need a minimum of 4 available satellites to solve for x, y, z and clock error to determine the position.

A Tropospheric error T, is the error due to weather effects, like water droplets causing refraction, water vapor and other atmospheric gases. This will cause an offset that needs to be accounted for *Saastamoinen* [1972]. The troposphere is not a despersive medium, so the tropospheric delay is not dependent on the frequency of the signal. The biases, $K_{P,r}$ and K_P^s, are the hardware delays for the receiver and the satellite as the devices can not process the information in real-time.

Multipath makes the signal travel further due to it being reflected off objects *Irsigler et al.* [2004]. This can be caused by a tall structure nearby, i.e. buildings and trees.

ϵ_p is white noise in the receiver which is due to thermal heat .

The ionospheric delay is the second highest error after the receiver clock. However, as the receiver clock error is handled automatically by all standard positioning algorithms (including single-frequency algorithms), the ionospheric delay is the largest error that requires more advanced handling. The ionospheric delay is the term α_fSTEC, where α_f is the conversion factor between the integrated electron density over the ray path, STEC (Slant Total Electron Content), and the signal delay at frequency f.

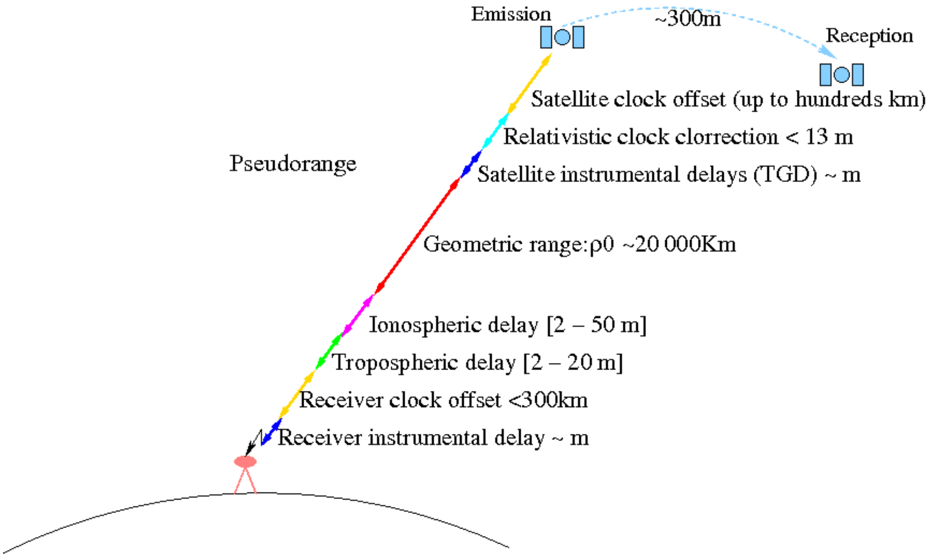

Figure 2.6: This is an illustration of the different error sources a signal encounters from the satellite experiences on the way to the GNSS-receiver. This makes the GNSS-receiver on ground measure a different distance than the actual geometric distance between the receiver and satellite. We can see delays such as ionospheric delay, Tropospheric delay, satellite clock offset, receiver clock offset, instrument delays and others that we will not go into in thesis. The Figure is from *ESA* `https://gssc.esa.int/navipedia/index.php/GNSS_Measurements_Modelling`.

The reason for the ionospheric delay is due to a different refractive index in the medium. Here the n is the refractive index, which is a part of the dispersion relation, $n = v/c$. This will tell us how fast the signal travels and this is vital to measuring the correct distance from the satellite to the GNSS-receiver. This index, n, can be calculated from the Appleton-Hartree equation *Pécseli* [2013b], see equation 2.5.

$$n^2 = 1 - \frac{X(1-X)}{1 - X - \frac{1}{2}Y^2 sin(\theta) \pm \sqrt{(\frac{1}{2}Y^2 sin^2(\theta))^2 + (1-X)^2 Y^2 cos^2(\theta)}} \qquad (2.5)$$

Here X is defined as $X = \frac{\omega_{pe}^2}{\omega^2}$, where ω is the angular frequency of the signal sent through the medium and ω_{pe} is the plasma frequency of the medium. The plasma frequency is defined as $\omega_{pe} = \frac{e^2 n_e}{\epsilon_0 m_e}$, where the e is the electron charge, n_e is the density of the electrons and m_e is the mass of the electron. Y is defined as $Y = \frac{\omega_{ge}}{\omega}$, where ω_{ge} is the electron gyrofrequency as in a magnetic field the electron gyrates, see *C.T. Russel and Strangeway* [2016]. However, Y can be set to 0 as the gyrofrequency is very low compared to the frequency of the signal. Giving us $n^2 = 1 - \frac{X(1-X)}{1-X} = 1 - \frac{\omega_{pe}^2}{\omega^2}$.

So the plasma concentration is the main fluctuating term and it can vary due to sources such as ionization of the ionosphere and particle precipitation. So as the refractive index depends on the plasma, so will the velocity of the signal also be influenced by the plasma concentration. Therefore, as a different velocity will output a different position, the distance measured is correlated with the plasma concentration in the ionosphere.

b Phase measurement

A GNSS receiver measures delay by looking at what time the signal is sent. It also measures the phase of the signal. This measurement is more accurate than pseudorange, but a combination is used in the standard GNSS-receivers. We can write equation 2.4 based on phase instead of distance, which can be seen in equation 2.6.

$$\Phi_L = \rho + c(dt_r - dt^s) + T - \alpha_f \text{STEC} + k_{L,r} - K_L^s + \lambda_L N_L + \lambda_L w_L + m_L + \epsilon_L \tag{2.6}$$

In equation 2.6, $\Phi_L =$ is the Carrier Phase measurements, which measures which part of the phase the signal is at when received. However, with equation 2.6, it cannot detect how many cycles have occurred since it was transmitted. This is represented as the Integer ambiguity, λN. In addition to the integer ambiguity, there is an extra term $\lambda_l w_L$, which is the wind up due to circular polarization of the electromagnetic signal.

Equation 2.4 and 2.6 are similar, but have a few notable differences. We have in addition $\lambda_l w_L$, which is the wind up due to circular polarization of the electromagnetic signal.

c Ionospheric measurements

TEC

Today most GNSS-receivers use two frequencies for increased accuracy. As we can see in equation 2.7, the ionospheric delay of the signal is dependent on the frequency. If two signals is sent at the same time with different frequency through the ionosphere, we can use that they take different amount of time to reach the receiver. By observing the difference in time and using that only the ionosphere in equation 2.4 is affected by the frequency of the signal, we can estimate the ionospheric delay. In addition, it is also possible to model the ionosphere using GNSS receivers *Hernández-Pajares et al.* [2011].

$$\triangle I = \alpha_f \text{STEC} = \frac{40.3}{cf^2} STEC \tag{2.7}$$

Equation 2.7 tells us about the delay of the signal, where $\triangle I$ is the ionospheric delay, STEC is the slant total electron content, c is the speed of light and f is the frequency of the signal. Here the STEC is not the same as TEC, as usually the satellite measures the receiver from an angle. However, when we model the ionosphere, we can from approximate the TEC values from the STEC.

ROTI

A GNSS-receiver can adjust for a given TEC value using dual frequencies, but a changing TEC value can be challenging for the receiver to adjust for. Therefore we can take a look at the changes in TEC, namely ROTI (Rate Of TEC Index). ROTI has been found to be a good measure of disturbance as they are typically associated with scintillation *K.S. Jacobsen* [2012], *Basu et al.* [1999]. ROTI is calculated by using equations 2.8, 2.9 and 2.10.

First we have the geometric free phase observations at time i in equation 2.8. Φ_{L1} and Φ_{L2} is the phase measurements for the two different signals.

$$L_{GF}(i) = \Phi_{L1} - \Phi_{L2} \tag{2.8}$$

$$\text{ROT} = \frac{L_{GF}(i) - L_{GF}(i-1)}{\triangle t \times 10^{16} \times 40.3 \times (\frac{1}{f_1^2} - \frac{1}{f_2^2})} \tag{2.9}$$

In equation 2.9, $\triangle t$ is the time difference between epochs, f_1 and f_2 are the two signal frequencies. Then we have the ROTI as the standard deviation of the ROT (Rate Of TEC):

$$\text{ROTI} = \sqrt{\langle ROT^2 \rangle - \langle ROT \rangle^2} \tag{2.10}$$

As seen in equation 2.7, the delay is dependent on the frequency of the signal. As it is mainly the ionosphere which has this frequency dependence, we can use it to calculate the TEC by looking at the difference in the delay between two frequencies.

d Scintillation

A receiver is equipped to adjust for constant delays, but a changing delay is difficult to fully account for. In high latitudes that we are looking at in this thesis, there are polar precipitation and polar cap patches, which are known to cause scintillation. *Kersley et al.* [1995], *Burston et al.* [2010], *Skone et al.* [2009], *Aquino et al.* [2005], *Aarons* [1997], *Carlson* [2012]. Scintillation is a disturbance of the GNSS-signal due to the ionosphere. These occur when we have plasma irregularities with small structures, which are common in the ionosphere *Hey et al.* [1946],*Yeh and Liu* [1982]. These irregularities are typically increased during storm activity as they can be created by a GDI (Gradient Drift Instability) *Basu et al.* [1990] or a KHI (Kelvin Helmholtz Instability) *Spicher et al.* [2020]. These irregularities causes a highly fluctuating TEC value and since the signal delay in the ionosphere, as described in equation 2.7, is dependent on the TEC, the delay is highly fluctuating as well.

The scintillation can decrease the accuracy of the GNSS-receiver or completely make the GNSS-receiver unable to get a fixed position. There are two main types of scintillation, phase scintillation and amplitude scintillation *Kintner et al.* [2007]. In order to measure these we use the scintillation indices, S_4 and σ_ϕ *Fremouw et al.* [1978]. The phase scintillation index, σ_ϕ, is the standard deviation of the detrended carrier phase and is used to characterize the phase scintillation activity. For amplitude scintillation, we use the amplitude scintillation index, where we take the standard deviation of the signal power to the mean signal power.

$$\sigma_\phi = \sqrt{\langle \phi^2 \rangle - \langle \phi \rangle^2} \tag{2.11}$$

$$S_4 = \sqrt{\frac{\langle I^2 \rangle - \langle I \rangle^2}{\langle I \rangle^2}} \tag{2.12}$$

Here $\langle\rangle$ denotes the average over 60 seconds. They also both are filtered by sixth order low pass Butterworth filter *Van Dierendonck et al.* [1993].

At polar latitudes, phase scintillation is more commonly observed than amplitude scintillation *Kersley et al.* [1995]. We also know from statistical studies that phase scintillation occur co-located with the auroral region *Jin et al.* [2015], *Tiwari et al.* [2013].

e CPOS network

The system we utilize in this thesis is called CPOS (Centimeter POSitioning). It uses the network RTK (Real Time Kinetic) technique to assist users, leading to better results than a stand-alone GNSS receiver. It uses fixed base stations with a dual frequency GNSS-receiver to provide corrections within less than a second *Rizos et al.* [2009]. By using that the fixed based position have a known position, the base stations can calculate the error sources in equation 2.4 and 2.6. It can also model the ionospheric delay to provide better corrections for users between base stations. The CPOS system has base stations located evenly in Norway. Note that the closer the user of the CPOS system is to a base station, the better it will function. This is because the interpolation function have reduced accuracy the further away from a base station *Lejeune et al.* [2012]. The base stations can be seen in Figure 2.7.

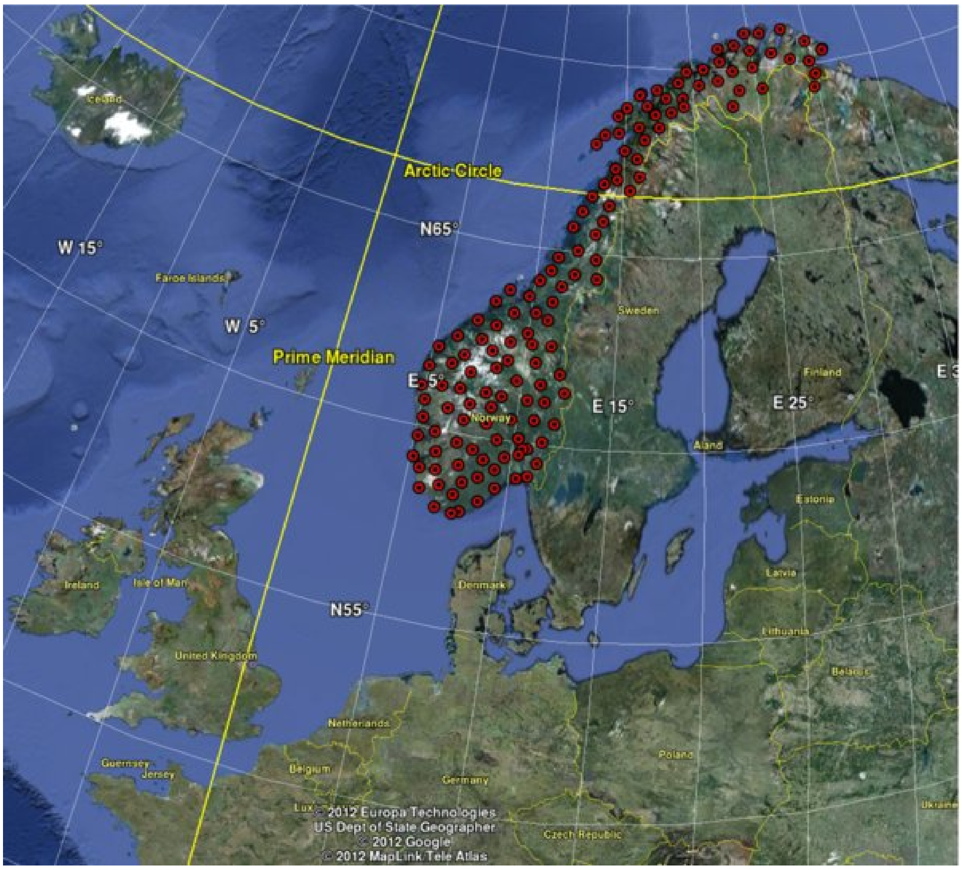

Figure 2.7: This is the CPOS network in Norway. This system helps to provide users with a highly accurate position. The red dots represent the base stations which have a fixed dual frequency GNSS receiver that help a user. Figure from *K.S. Jacobsen* [2012].

The data from the GNSS receiver network, provides ionospheric measurements and create a map of the ionosphere both for TEC and for ROTI. This can provide further knowledge for the user as it can show if the measurements have been affected by space weather. This also provides great means to further study both the ionosphere and how GNSS responds during storm activity. There is currently live measurements of ROTI done by the NMA (Norwegian Mapping Authority), which is available at the site `sesolstorm.kartverket.no`.

Chapter 3

Method

The processing tools for this project can be found in the GitHub-repository [1] Here we will first go through each of the data sources; magnetometer that measures magnetic fluctuations, ROTI data that looks at changes in plasma in the ionosphere and NMEA GNSS data that tells us the accuracy of the CPOS system. We have decided to look at instruments in Northern Norway as particle precipitation occurs more frequently in high latitudes than in the equatorial regions, see *Basu et al.* [2002]. Therefore we have picked the Tromsø magnetometer, Tromsø GNSS-receiver and ROTI map data located in that region. We will then look at the SuperMAG event times, with respect to what they are, how they are made and how they have filtered. Afterwards, we go through how we perform a superposed epoch analysis on the data with the relevant times and the binning system that we use in this thesis.

3.1 Processing of the data sources

a Magnetometer dataset

For the magnetometer we download the data from SuperMAG website and look at the Tromsø magnetometer. The measurements are averaged over a minute period to subtract from the background magnetic field of the Earth. This provides us with a point for almost every minute for the year of 2018. This will be used to measure the substorm activity.

b ROTI dataset

ROTI calculations can be seen in the GNSS theory section. We decided to use a ROTI, where the measurements have a cutoff angle at 5 degrees. The cutoff angle is the angle, measured from the horizon ,0 degrees, to directly

---

[1] `https://github.com/michaesb/master_thesis_CPOS_System`

above, 90 degrees, that determines which satellites will be included in the calculation. A low cutoff angle, so more satellites closer toward the horizon will include more disruptions to the GNSS-receiver caused by e.g. vegetation and buildings which may lead to multipath. The measurements will be more similar to a user on the ground. By providing multiple measurements of ROTI from many stations and to each satellites, one can create a 2D map of the ROTI and interpolate the gaps in the map. In Figure 3.1, we can see two examples of the map data created by the NMA (Norwegian Mapping Authority).

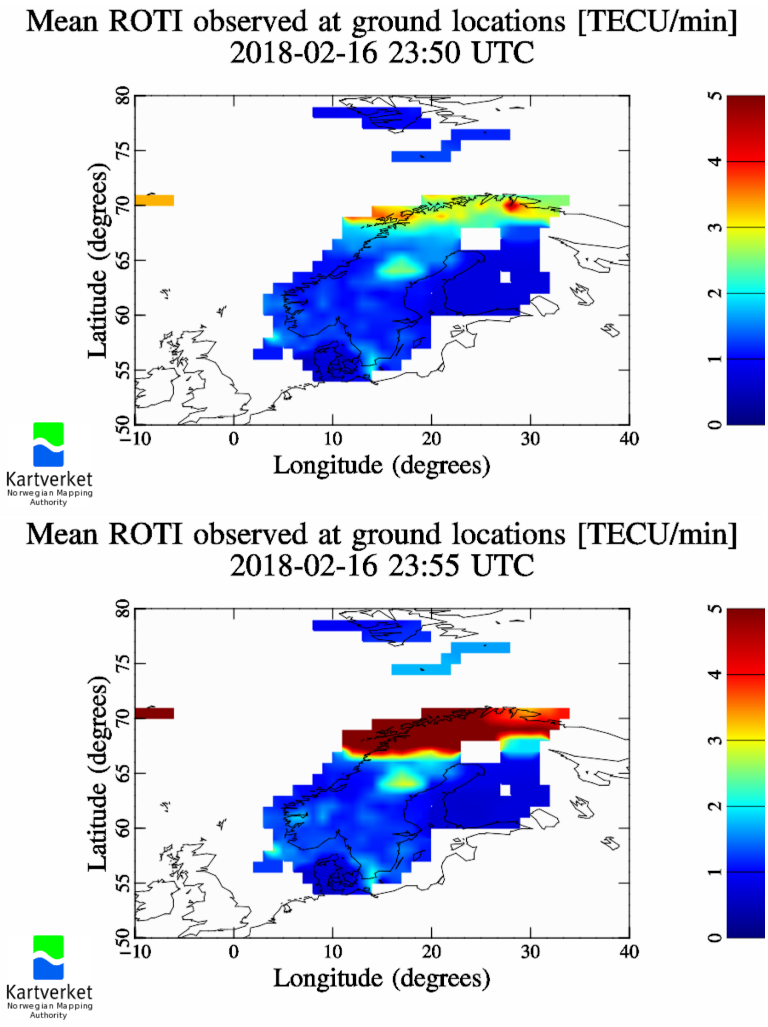

Figure 3.1: Here we can see two maps of Norway that shows ROTI measurements done by the NMA. The top is taken at 23:50 at February 16 2018 and the bottom one is taken 5 minutes after the previous image. We can observe low values of ROTI in southern Norway, but have increased values in Northern Norway. In the lower map the ROTI values are even higher for Northern Norway. These are taken from NMAs website ©Kartverket `https://sesolstorm.kartverket.no/` from their archive.

Since we are interested in a specific location, namely the Tromsø area in Northern Norway, we will use Bilinear Interpolation to calculate the ROTI value for a specific latitude and longitude.

Although used more extensively in image processing, it can be used here to take a grid data and calculate the value of a point between the grid points. The point value can be extracted by using the 4 surrounding points and then weighted by how close it is to each point. Figure 3.2 is an illustration that shows how this can be done.

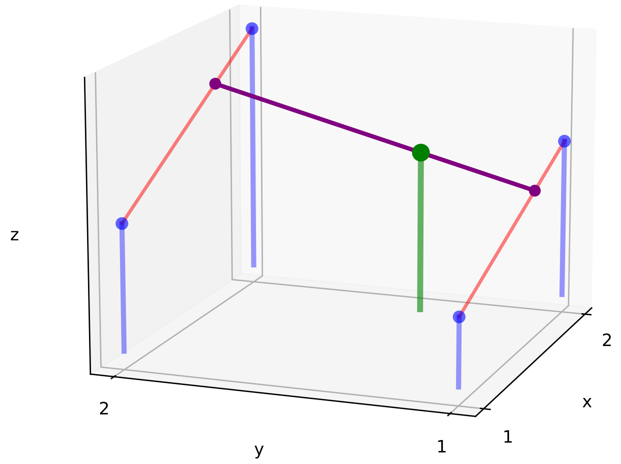

Figure 3.2: Here we see a visualization of the bi-linear interpolation method.This method can estimate the data in a point, by using the surrounding points. In this example plot, the green point [1.7,1.34] is interpolated. We have visualized this by drawing two supporting lines between the points in the x direction for the neighboring points. Then a line is drawn in the y direction from the two supporting lines that intercepts the desired position.

The map data in Figure 3.1 has the resolution resolution of 1 degree in both latitude and longitude, which is quite coarse for our measurements. For this thesis, we would like to know the ROTI value in position at 69.66, 18.94 degrees, which is the location of the magnetometer and the GNSS-receiver in Tromsø. Therefore, we use Bilinear interpolation to extract the values from that point to get the relevant value from the position of the magnetometer and GNSS-receiver.

c Calculating the noise from the GNSS-receiver

For noise calculations, we extract data from a GNSS-receiver located in Tromsø. This receiver uses the CPOS service in the same way as a human user would, but the receiver is in a fixed position. To see how accurate the GNSS-receiver is, we look at the position data. Since the GNSS-receiver is in fixed position, any movement measured will be due to disturbances. To measure the disturbance, we calculate the noise by using rolling standard deviation 3.1 of vertical position z, as this was given in the NMEA files in meters. This lets us see how much the measured position varies from second to second.

$$\sigma = \sqrt{\frac{1}{N-1} \sum_{t_i-\Delta t/2}^{t_i+\Delta t/2} |z(t_i) - \bar{z}|} \tag{3.1}$$

Here z(t_i) is the position at time t_i, $\bar{z}$ is the average position over time $\Delta t = 60$ and N is the number of points.

Processing GNSS noise data

As an example of the type of data we use, we show in Figure 3.3 and 3.4, the three data sources we use. Top plot is the magnetometer data, with red dots to show the event times, which we will later get into. In the middle is the ROTI measurements and the bottom has the GNSS measurement. In the Figure period from May 31 to June 4 of 2018, we see a large increase in the base noise level of GNSS data.

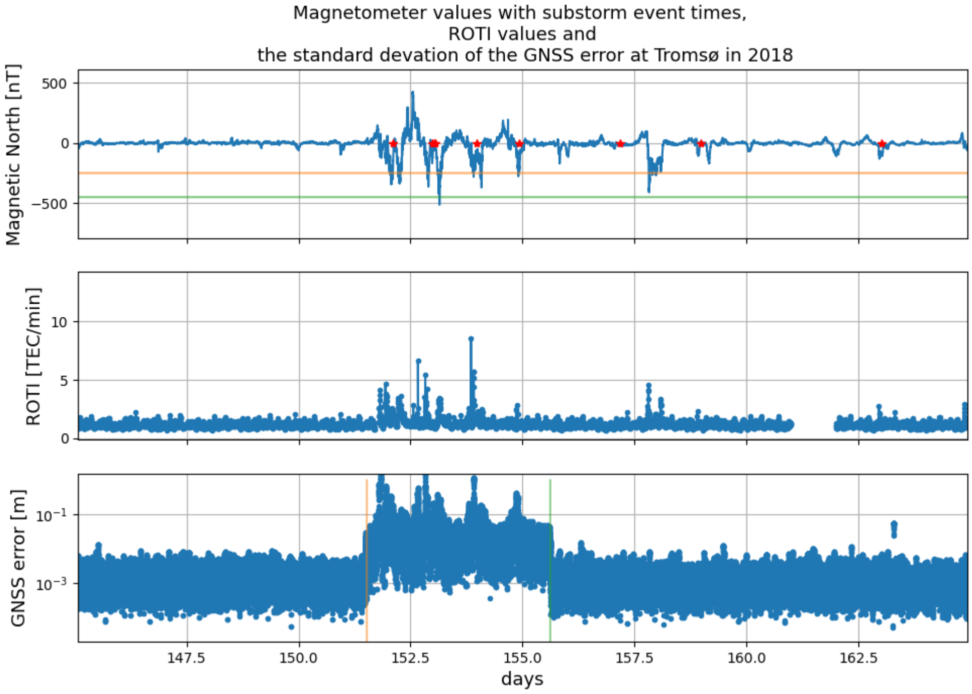

Figure 3.3: Here are the 3 data sources, Magnetometer, ROTI and GNSS noise. The magnetometer has the event time as red dots to show the selected the event times. The magnetometer plot has an orange line to show the difference between weak and moderate substorms and a green line to differentiate between a moderate and strong substorm. This defined in the result section. Here we show the GNSS noise before it was corrected.

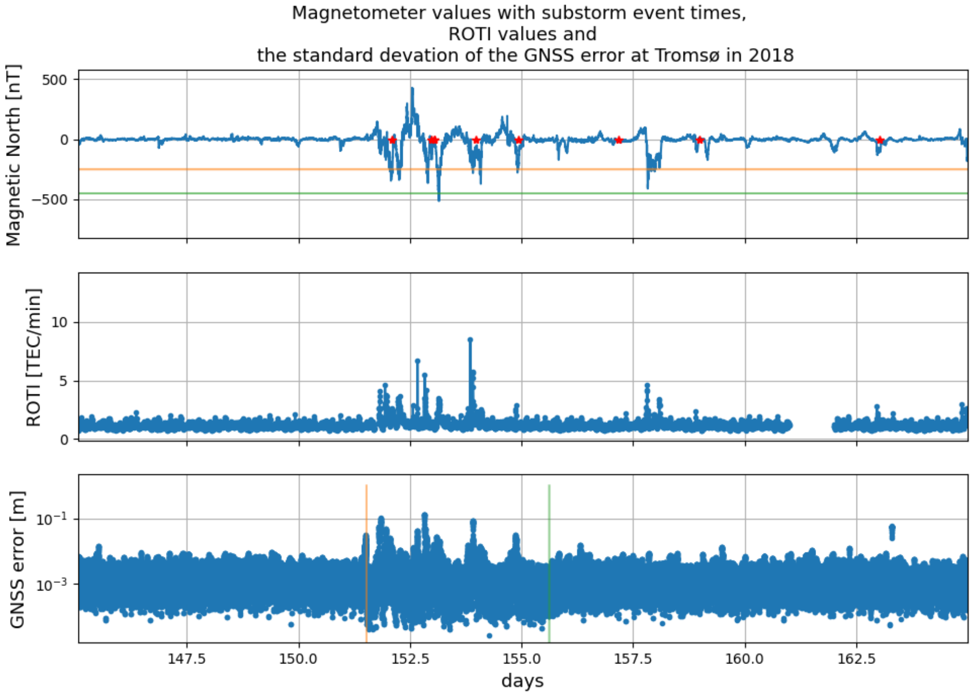

Figure 3.4: Here are the 3 data sources, Magnetometer, ROTI and GNSS noise. The magnetometer has the event time as red dots to show the selected the event times. The magnetometer plot has an orange line to show the difference between weak and moderate substorms and a green line to differentiate between a moderate and strong substorm. This defined in the result section. We have used an orange and green line in GNSS part to visualize the area we corrected and see that the plot looks normalized compare to the rest of the plot.

We are unsure of the cause of this increased noise level in this period, but we can see that there are relevant events that have a increased base noise level. Therefore, we have decided to do a statistical correction, where we divide the elevated data by the ratio = $\frac{median1}{median2} = 13.7$, where median 1 is the median value of the elevated data, and median 2 is normal base level for the noise. The start and stop of the heightened values was visually estimated from the plot.

The increased noise level is likely due to a technical error, as this occurs over multiple days, so it is unlikely due to the Sun or an atmospheric effect. We see in Figure 3.4 that in the bottom plot where we made the statistical correction that the events seem to be intact despite the error, so the 4 events are worth including in this dataset.

3.2 SuperMAG event data

a SML-index

As previously described in the Theory 2, the AE-index is a measure of Auroral Electrojet activity. However, the AE-indices uses only 10-13 magnetometer stations and according to *Davis and Sugiura* [1966a], this allows some substorms to pass through without being detected. We will therefore look at the SME-indices, which use approximately 300 magnetometer stations and therefore can better identify substorms.

In Figure 3.5, we can see the different magnetometers used by the AE indices in blue and SME indices in red and blue.

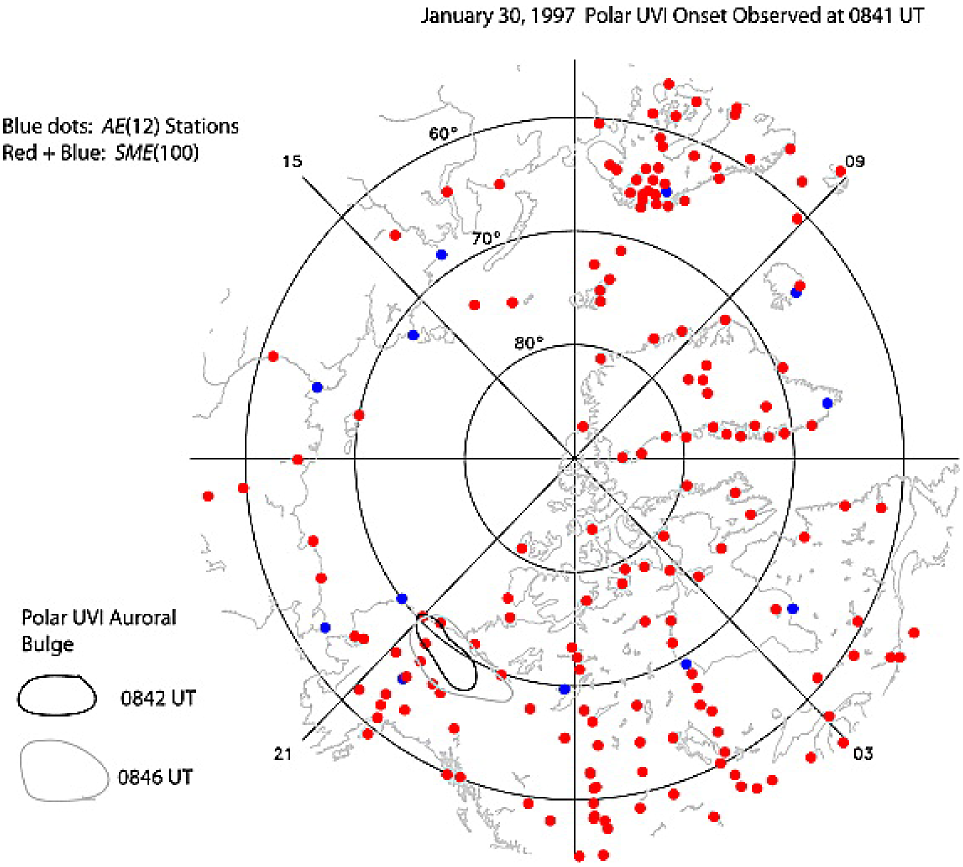

Figure 3.5: Here we can see the collection magnetometers in the northern hemisphere, where blue is the stations used by AE-indices and red and blue is the stations used by SME-indices. Although there are only a 100 visible stations in this image, the SME-indices uses roughly 300 stations.This image is taken from the article *Newell and Gjerloev* [2011], `https://doi.org/10.1029/2011JA016779`.

The SME-indices have the same naming conventions as the AE-indices, i.e. SMU is the highest value of the magnetometers, SML is the lowest value of the magnetometers and SME = SMU - SML.

b Acquiring a list of substorms

The SuperMAG website provides a list of substorms `https://supermag.jhuapl.edu/substorms/`. The website uses the criteria from *Newell and Gjerloev* [2011] to generate a list of substorms that occur around the high latitudes. The criteria uses the SML, which is the lowest value of the magnetometers, as this captures the substorm onset.

The criteria can be seen in equations 3.2, 3.3, 3.4, 3.5. The 3 first criteria are to have a sufficiently sharp decline in the SML, and the fourth one is to make sure the graph has a sustained sufficient overall drop.

$$\mathrm{SML}(t_0 + 1\,\mathrm{min}) - \mathrm{SML}(t_0) < -15\,\mathrm{nT} \tag{3.2}$$

$$\mathrm{SML}(t_0 + 2\,\mathrm{min}) - \mathrm{SML}(t_0) < -30\,\mathrm{nT} \tag{3.3}$$

$$\mathrm{SML}(t_0 + 3\,\mathrm{min}) - \mathrm{SML}(t_0) < -45\,\mathrm{nT} \tag{3.4}$$

$$\sum_{i=4\,\mathrm{min}}^{i=30\,\mathrm{min}} \mathrm{SML}(t_0 + i)/26 - \mathrm{SML}(t_0) < -100\,\mathrm{nT} \tag{3.5}$$

Here t_0 is SML onset time for a substorm. Note that the algorithms require a minimum of 30 minutes worth of measurements ahead of onset. These criteria are chosen because we are looking for a downward fall in the SML magnetometer.

Equation 3.2 requires that the magnetometer to dip below -15 nT after 1 minute, equation 3.3 requires that the magnetometer to be below -30 nT after 2 minutes and equation 3.4 needs a dip below -45 nT after 3 minutes. The fourth criteria requires the average value to be below -100 nT for the rest of the 30 minutes after the onset.

c Filtering

The Auroral electrojet can occur anywhere at high latitudes, i.e Russia, Canada and Greenland, but we will narrow it down to Norway. In order to do this, we have filtered based on what latitude the storm is located at and at what time. We can get the latitude by looking at what latitude the magnetometer measures the current. The time filtering will select what longitude we are observing. Since we know that substorm occur during night time, we can filter out the substorm occurring during the day for Norway.

We decided to select the events between 20 and 4 in UT +1, which is the local time for Norway.

The last criteria is due to a big data gap in the GNSS data likely caused by downtime or some technical difficulty of the GNSS-receiver. To adjust for this we ignore the data from other sources as well on that time period.

- the time between 20 and 4 at night (adjusted for UT+1 for Norway)
- latitude between 58 and 71 degrees
- no repeats of events that are close together, to avoid duplicates.
- filtered by the GNSS-receiver noise missing data

Figure 3.6 shows an example of how the event times fit with magnetometer and the other data sets. The red dots is the event times which is partially filtered. The orange horizontal line signifies the difference between a weak and moderate substorm and the green line is difference between moderate and strong storms. The Figure illustrates that there are event times that are close together,i.e. approx day 83, showing a need for filtering this out. Also note that some of the data gaps of the GNSS-receiver are small like one hour or in some cases a full day, but there is a big gap that lasts for 77 days, from September 29 to December 8. There is a table in the appendix B.1, that says how many events are removed by each filtering criteria.

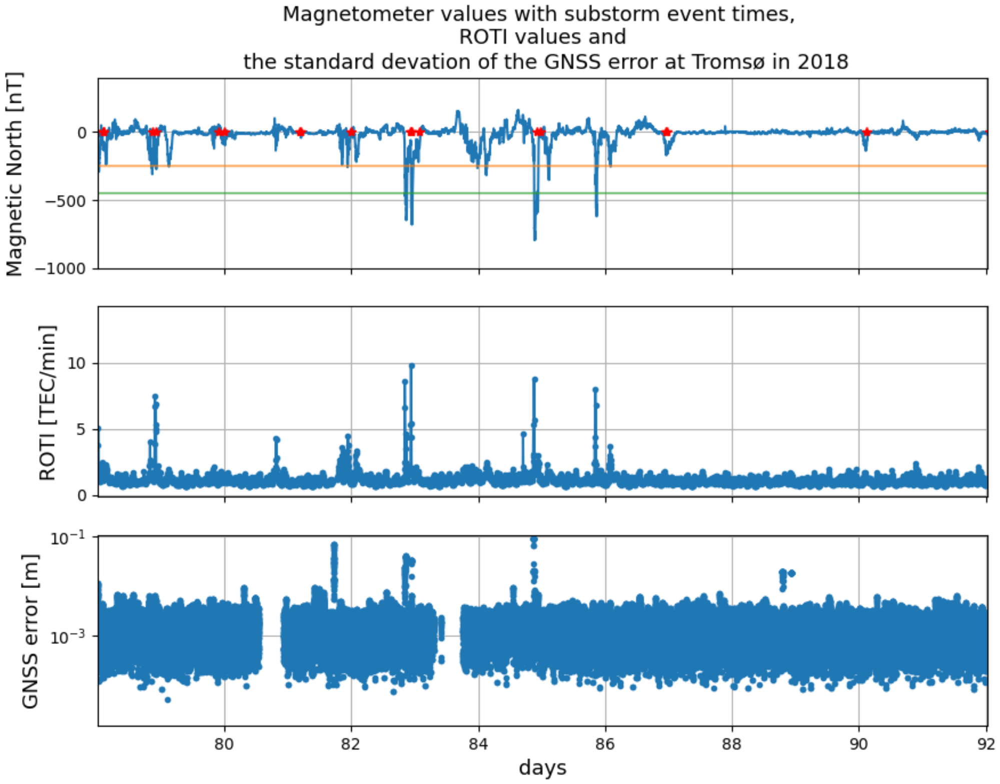

Figure 3.6: Here we have plotted the data sources from day 79 (20th of March 2018) until day 90 (31th of March 2018). At the top, we have plotted the magnetometer data with event times shown by red dots. Note we have only partially filtered the event times here, so it does not have filtering for duplicates and for datagaps. The orange horizontal line signifies the difference between a weak and moderate substorm and the green line is difference between moderate and strong storms. The weak substorm is the bottom third of the magnetometer output, moderate is the middle third and the strong is top third. The middle plot is the ROTI data at Tromsø and afterwards is the GNSS noise data.

We notice that the red dots in 3.6, which are the event times, coincide with drops in magnetometer graph, which is promising for a functional event finder.

3.3 Superposed epoch analysis

Now that we have relevant times for potential substorms and relevant data sources, we choose a 4 hour window, 1 hour before the time and 3 hours after each dataset. This lets us see the start of the event and its effects. However a lot of these events are not a perfect example of a substorm as they might have some false positives that evaded the filter we have used, technical problems on the instruments and other space weather effects other than the substorms that give an incomplete picture of the substorm. To account for these outliers, we have used Superposed epoch analysis. In Superposed epoch analysis, we can average time series of key events, in our case substorms, to see how they act as whole. This is done by adding the measurements in a single plot and then looking at the average or median value of measurements done by an instrument. This is then repeated for each type of instrument. This allows us to look for trends in the data, so to better see the core behavior of what we wish to observe.

In this thesis, we have chosen to add all of the measurements from the magnetometer in the same plot with median line, 95th percentile line and 5th percentile line. This is also done for the ROTI and the GNSS-error. We chose to use the median values to plot the result, instead of averages to lessen the effect of big outliers and spikes in the data. We also looked at percentiles 95 th and 5 th to see what extremes we see in the data as this will be the threshold for the really disruptive substorms and the very weak substorms or false positives substorms.

3.4 Binning system

In this thesis we have sorted the event times on the basis on the magnetometer data. As described in the theory section, a substorm can cause a negative spike in the magnetic north component of the data. The larger the spike the stronger the current and it indicates how severe the substorm is at Tromsø. Therefore we have sorted the event times based on the minimum value of the magnetometer for the 4 hour period.

In addition to this we have have divided the data into three bins; weak bin, medium bin, strong bin. The bins have the same number of events in them, but the first bin will have the event times with the smallest magnetometer impact, the second bin will have the event times with the medium magnetometer impact and the third bin will have the strongest magnetometer impact.

Note that this not only sorts the magnetometer data, but also will be the same order for the ROTI and the NMEA dataset. We will utilize the bin system with ROTI and NMEA dataset as well.

Chapter 4

Results

4.1 Event time distribution

In this thesis, we have used 197 event times after filtering, which puts approximately 65 events in each bin. Figure 4.1 illustrates the bin system, showing the distribution of the minimal magnetometer values. The weak bin has magnetometer values at -259.9 nT or above, medium bin has values between -256.9 nT and -430.6 nT and the strong bin is below -430.6 nT.

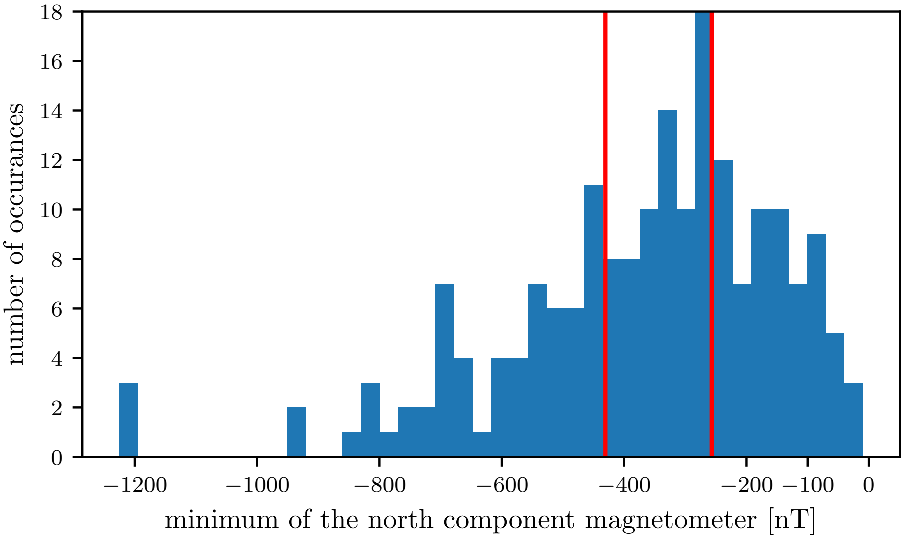

Figure 4.1: This plot shows event times with corresponding minimal magnetometer values over 4 hour period. The red lines are the separation between the bins, where the right section is the weak bin, medium bin is the middle and strong bin is the left section. Note that the bins have 65 events each.

In Figure 4.1, we can see that the majority of the data is between -800 and 0.

Figure 4.2 is a plot of the distribution of latitudes where the substorm occurs. The median value is at about 67 degrees, while Tromsø is at approximately 69.6 degrees latitude. The maximum value of the columns is at approximately 58 occurrences. There are few substorm measured below 63 degrees latitude, which approximately where Trondheim is.

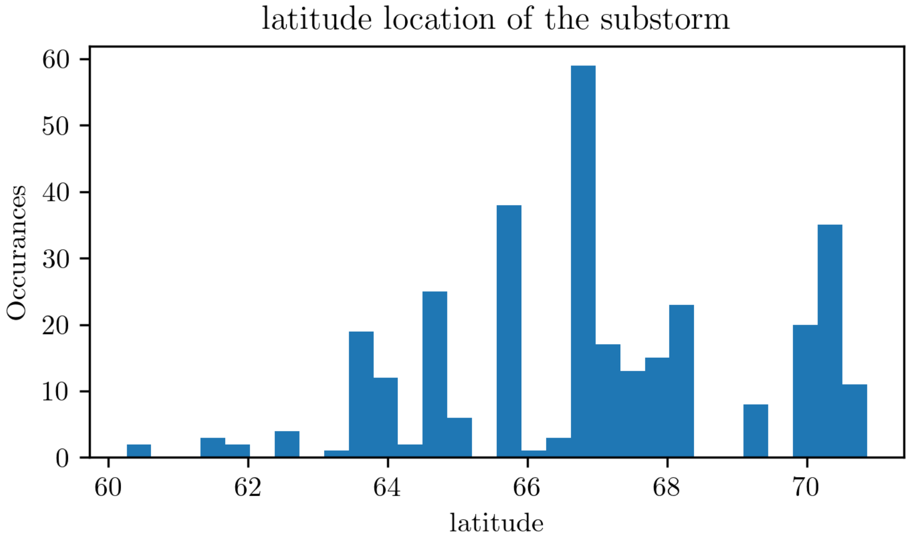

Figure 4.2: Here you can see the distribution of the location of the substorms, measured by latitude. This is the filtered list specific for Norway. We can see a trend for substorm happening more frequently in higher latitude

4.2 Superposed Epoch analysis

Here we compare the superposed epoch analysis of each of the instruments in the same figure using the provided SuperMAG evenlist from *Newell and Gjerloev* [2011]. Figure 4.3 shows all the event times. Figures 4.4, 4.5, 4.6, shows the weak bin, medium bin and strong bin. All of the figures have a median line, 95th percentile line and 5th percentile to better show trends. The event time is 0 on the x-axis, with a blue line to highlight this. The start is at -60 minutes before the event, and the end at 180 minutes,which is 3 hours past the event time.

In the magnetometer part of the figures 4.3 ,4.4, 4.5, 4.6, there is a median line and 5th percentile line, that move in the negative direction at time 0 and reaches a minimum value at about 20-25 minutes. From there it slowly moves towards 0 nT and takes about 2 hours to reach values from before the event. In Figure 4.6 we can see this occur with 95th percentile as well. As we go from weaker to stronger bins, the dip is increasing.

The ROTI part of the Figures 4.3 ,4.4, 4.5, 4.6 shows a increased value at time 0 with the median line and is stronger with the 95th percentile. The peak value is reached at 15 minutes after onset for all figures. The 95th percentile has the peak at approximately the same place, but the 95th moderate and strong bin does not have sharp peak shape and are more chaotic. Both the peak value and duration of the peak increases as you go from the weak bin to the strong bin.

The GNSS-accuracy part of the Figures 4.3 , 4.5, 4.6 have a peak value in the 95th percentile at approximately time 15 minutes after onset. This is not including the weak bin. This peak value is stronger in the strong bin compared to the medium bin.

Note that in Figure 4.3, the GNSS-error peak and the ROTI peak coincide at the same time, however this does not occur for the magnetometer peak. The magnetometer dip lasts for about 2 hours, but the ROTI peak has a duration of about 10-20 minutes. The GNSS-error is even shorter with approximately 5 minutes duration and is only visible in the 95th percentile.

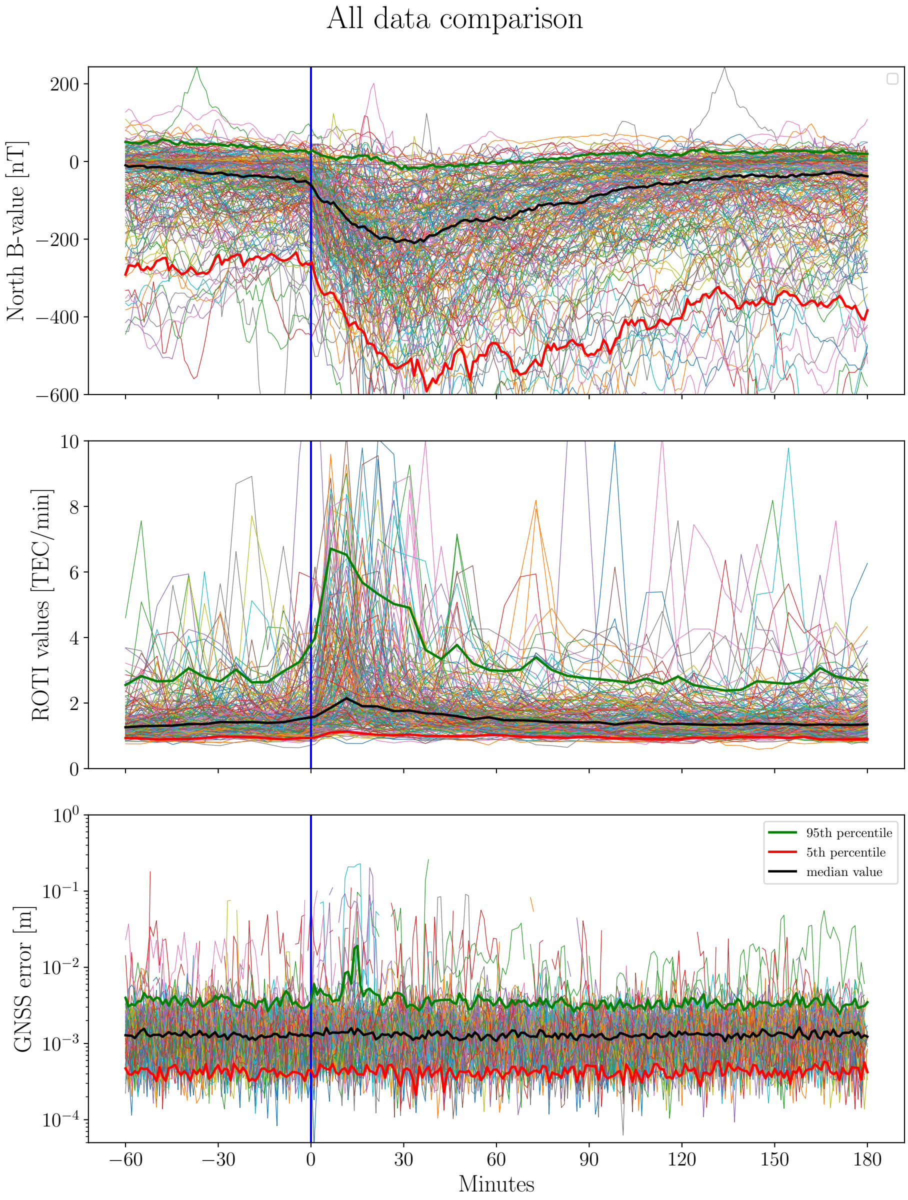

Figure 4.3: Here we compare all data sources; Magnetometer, ROTI and GNSS noise, with the same time axis. This is with the full dataset, where the thick green line is the 95th percentile of the full substorms, the thick black line is the median value and the thick red line is the 5th percentile. A vertical blue line is provided to better see the start of the event time as picked by the SuperMAG event list.

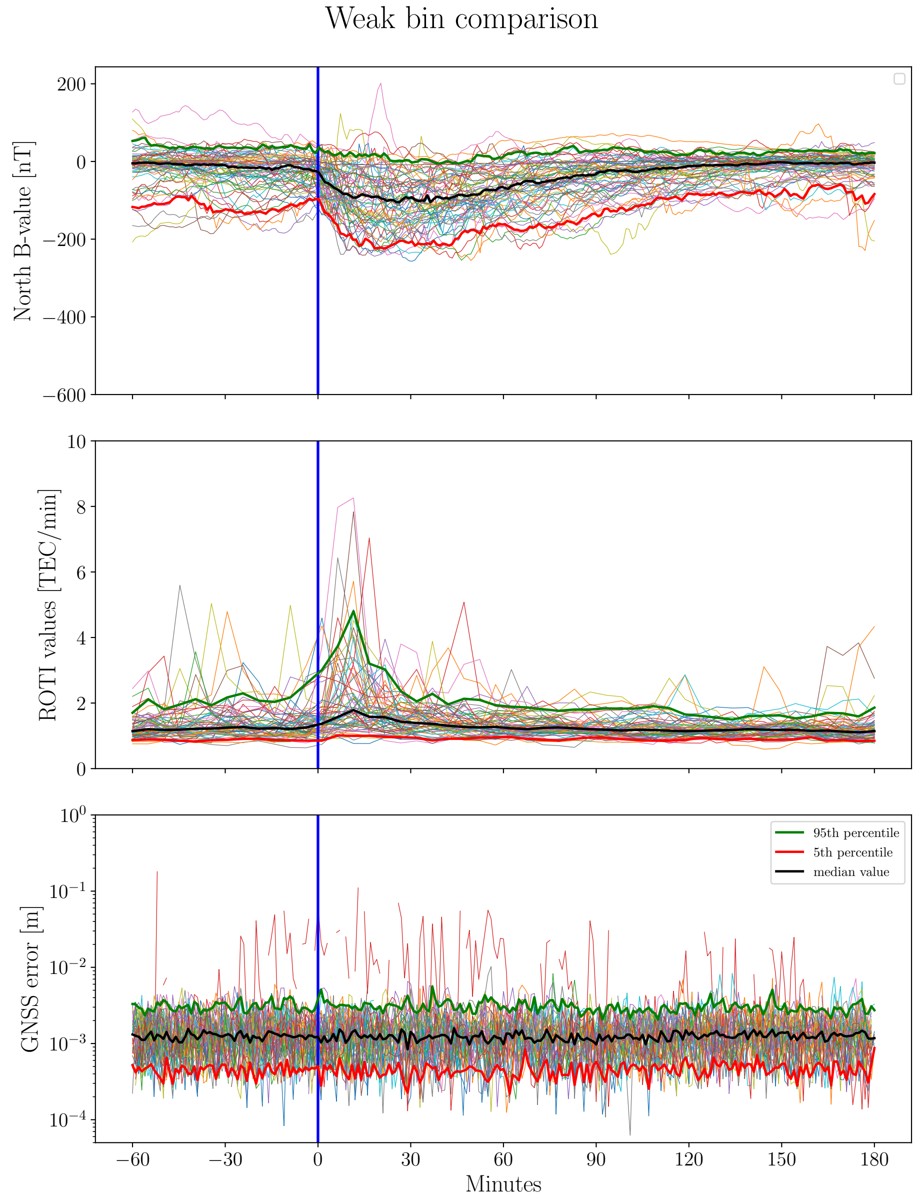

Figure 4.4: Here we compare all data sources; Magnetometer, ROTI and GNSS noise, with the same time axis. This is with the weak bin, where the thick green line is the 95th percentile of the weak substorms, the thick black line is the median value and the thick red line is the 5th percentile. A vertical blue line is provided to better see the start of the event time as picked by the SuperMAG event list.

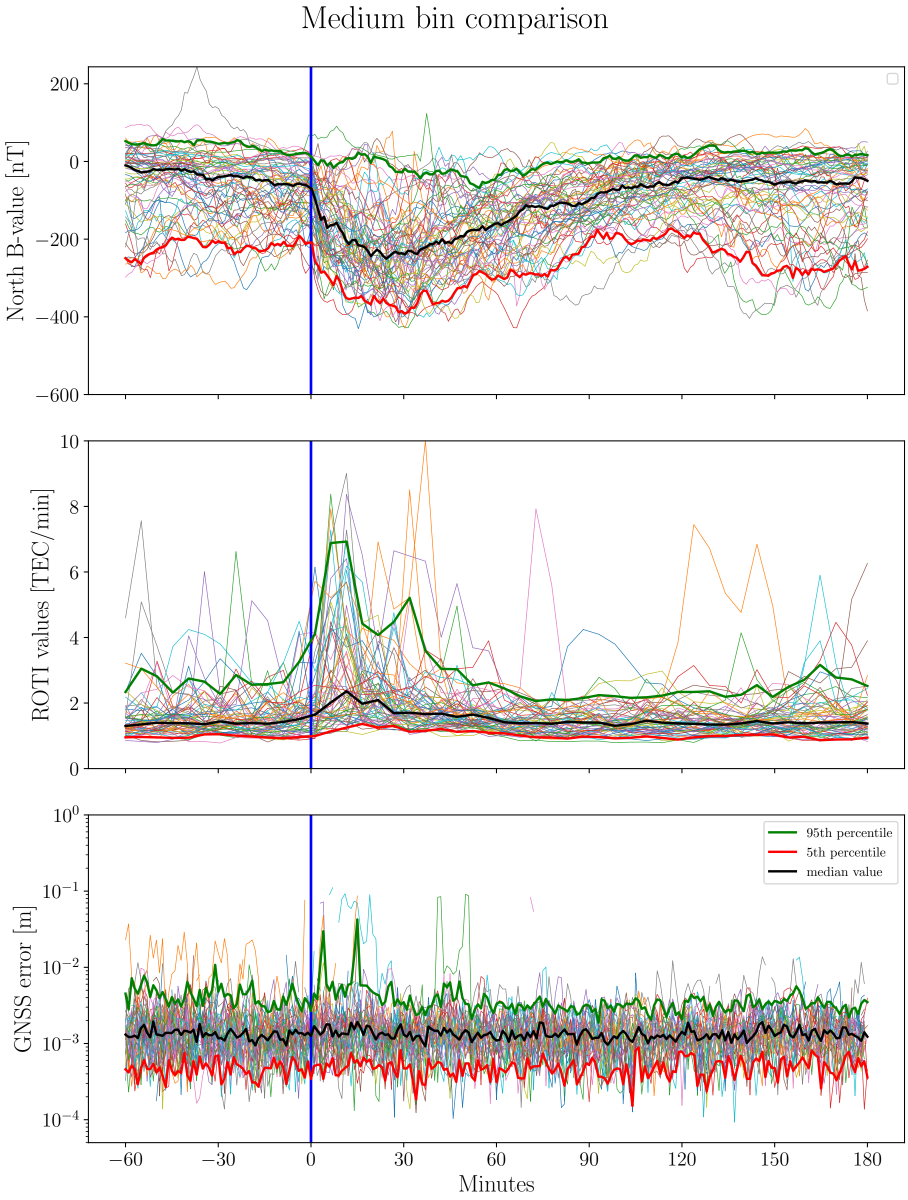

Figure 4.5: Here we compare all data sources; Magnetometer, ROTI and GNSS noise with the same time axis. This is with the medium bin where the thick green line is the 95th percentile of the moderate substorms, the thick black line is the median value and the thick red line is the 5th percentile. A vertical blue line is provided to better see the start of the event time as picked by the SuperMAG event list.

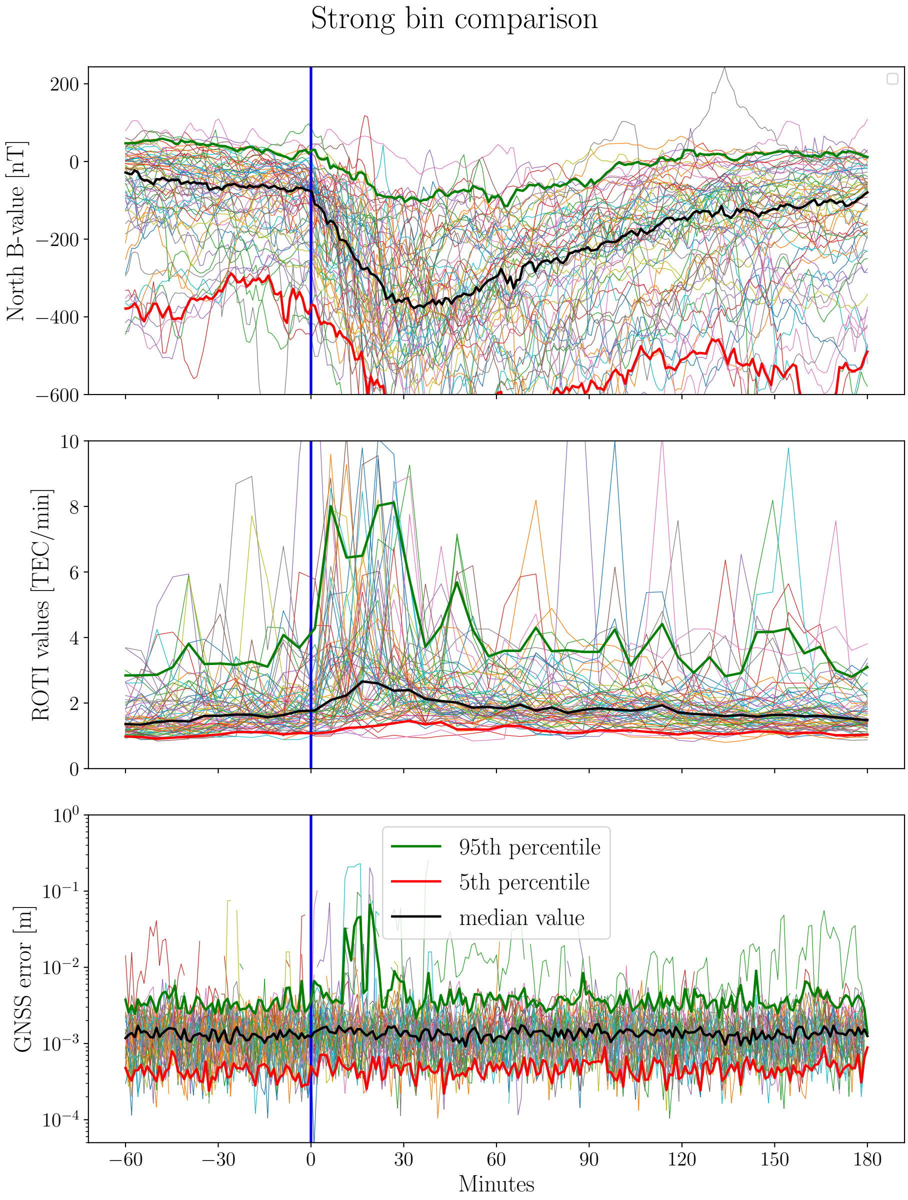

Figure 4.6: Here we compare all data sources; Magnetometer, ROTI and GNSS noise, with the same time axis. This is with the strong bin, where the thick green line is the 95th percentile of the strong substorms, the thick black line is the median value and the thick red line is the 5th percentile. Here there is a blue line to better see the start of the event time as picked by the SuperMAG event list.

Chapter 5

Discussion

We have for many years studied scintillation *Jin et al.* [2014], *Kintner et al.* [2007], *Jakowski et al.* [2012] as it was one of the earliest known space weather effects *Hey et al.* [1946] and scintillation has both been a way to study ionospheric phenomena and been a disturbance to GNSS usage. Here we look at a statistical analysis of substorms from 2018 given by the list in *Newell and Gjerloev* [2011], and look at three data sources to try to determine how the substorms affect the GNSS system in Northern Norway.

It is worth noting that 2018 is a year of solar minima (*National_Oceanic and Atmospheric_Administration* [2021]). This is relevant due to the fact that solar cycle affects the occurrence of scintillation *Y. Jin and Clausen* [2018]. Therefore we would expect to see less substorms or weaker substorms than one would on a year of solar maxima. We choose 2018 as we wanted to look at how the system performs in the most recent data that was available at the time. However, it would be interesting to see this statistical analysis done on a solar maxima instead, but then we have to wait for 2026, or see older data from around 2014.

5.1 Event times

In Figure 4.1, there is the minimal magnetometer value of the 4 hour duration for all substorm events found. In the distribution, the most frequent values are around -300 nT, but the distribution expands even further to -800 nT. This indicates that we have successfully picked relevant substorm times for our location, as this is a considerable increase, suggesting a substorm occurs. Since these substorms occur all over the northern hemisphere, we will record a lot of events that do not effect the GNSS-signals in Northern Norway, so a filtering algorithm is required. we do see however some values that are above -100 nT, that are unlikely to be relevant events for Northern Norway. This shows that the filtering is not fully successful and could be improved. A suggestion on how one can filter the weak substorms is to remove the substorms that are above a certain threshold of minimal magnetometer values, as this can give relevant substorms for a use case. One can also try the algorithm for detecting substorm specifically for the Tromsø magnetometer instead of the SML-index, but the algorithm would likely need some adjustments to work for a singular magnetometer.

In the superposed magnetometer plot, which is a part of the Figure 4.3, the graph has a clear trend at time 0 for the median line and the 5th percentile line. This is an increase of southward magnetic field that indicates a current being set up in the westward direction. This is consistent with a substorm happening and measuring the Auroral Electrojet with the magnetometer. The filtering, appears to be successful here as well, but can be improved, as there are some events in the 95th percentile that do not follow the median trend and can be false positives.

In the thesis *Ohtani and Gjerloev* [2020], they point out a flaw in the SuperMAG event list. They wrote in Appendix A:
"A similar technique was previously developed by Newell and Gjerloev [2011], who provided a complete list of substorms that could be used for statistical studies. However, we later found that their technique misidentified some events, and the onset timing was approximate. These shortcomings led us to develop a new technique with the purpose of providing a list of isolated events with a high degree of confidence."

This indicates that the list does have some false positives, as they mention some misidentified events. That is consistent with the events in the weak bin, as there is a considerable number that do not fit the median trend. The onset appears to be consistent at time 0, so we deem the onset time accurate enough for the superposed epoch analysis done in this thesis. Also, since this is a statistical study, we deem the list still valid for this thesis, but there is room for improvement with misidentified events. It would be interesting to do the same superposed epoch analysis with the same data sources, but with the new list from *Ohtani and Gjerloev* [2020] to see if we can improve the number of relevant substorms for the Tromsø station.

As mentioned earlier there are likely some false positives in the current dataset, but we are not able to tell much about false negatives. Some of the substorms that passed through either the SuperMAG event list or were removed by the filtering process, can be good candidates. We would like to identify all events if possible, so this is something worth looking into. We would like to be tested for more lists i.e *Ohtani and Gjerloev* [2020] or *Forsyth et al.* [2015], as they might find substorm that is missing in the list generated here and provide a list with less misidentified events.

One can check the data, with scintillation measurements, to look for higher phase scintillation as that is a typically associated with substorm activity, but can be caused by other sources as well. *Kersley et al.* [1995], *Aarons* [1997]. One could also see if Aurora is present at the events as this is a sure sign for substorm activity *Aarons* [1997]. However searching for Aurora has a lot of difficulties, i.e. Midnight Sun during the summer in northern regions and cloudy weather that would render it impossible to classify a lot of of the substorms.

There may also be some bias in the events selected. In the paper *Ohma et al.* [2021], they investigate the occurrence of substorms where they find a correlation between a positive B_y of the solar wind and substorms. It was explained to be a result of how the magnetometers are mostly located in the northern hemisphere and it was an affect of the local hemisphere. The few magnetometers in the southern hemisphere showed the opposite to be true; that a negative B_y was correlated to more substorms. This means the algorithm is biased in northern hemispheres for positive B_y-values. This shows it is locally dependent and could perhaps benefit from either more stations on the southern hemisphere or combining the list with more data sources that are not locally dependent like solar wind measurements. This might improve the method and let it be less susceptible against local effects.

In Figure 4.2, the distribution of substorm with respect to latitude is shown. This is specifically for Norway and we can see a higher concentration in Northern Norway, which is expected. However, we do not have enough events to confirm anything from this plot as bigger sample size is required.

For an algorithm such as this, it could be interesting to see if one can use it live in order to detect a substorm in the onset period. Unfortunately that is not possible with the algorithm used in this thesis, as it needs about 30 min of future data, before it can categorize the substorm and that is after the spike seen in the GNSS-noise plot, Figure 4.3. The SuperMAG event list can see a better fit to categorize previous substorms and make a dataset used for testing and verifying other methods.

a Magnetometer

The bins of the magnetometer shown in Figures 4.4, 4.5 and 4.6 and the main magnetometer plot 4.3, all show a southward trend with the median line and the 5th percentile line at time 0.

The medium and strong bin of Figures 4.5 and 4.6, however have their median line going down to -220 nT and -380 nT respectively. The stronger magnetic field points to a stronger current created by the substorm, a substorm occur closer to Tromsø or a combination. Regardless of the case, this is a significant event occurring and shows that the filtering and sorting shows promise in finding a good list of substorms of different severity.

b ROTI

Here the ROTI plot in Figure 4.3 shows a clear spike that starts about 10 minutes before the event time and peaks around 17 minutes after the event time both at median line and especially for the 95th percentile. This shows that there is an increase in turbulence in the ionosphere briefly after the event time. It increases the median line by 0.5 ROTI. In Figures 4.4, 4.5, 4.6 on the ROTI part, we can see that the weak bin has the smallest spike both on the median line and 95th percentile line. The spike and duration are increasing in the medium bin on both the median line and 95th percentile line and this is increased even more on the strong bin. This would make sense as a stronger or closer substorm to the Tromsø area. This would likely create more disturbances in the ionosphere over the Tromsø area and therefore explain the higher measured ROTI in this time period.

In the article *Jacobsen and Dähnn* [2014], they try to define how much ROTI causes a given GNSS-error on the PPP (Precise Point Precision) of the data, which is the post processed data 2 weeks after using IGS accurate orbit information and clock error reduction. For a more detailed description of PPP, see *Zumberge et al.* [1997] and *Kouba and Héroux* [2001]. In *Jacobsen and Dähnn* [2014] they performed statistic analysis of the year 2014 for multiple receivers in Norway, but this thesis mainly focus on TRO1. They found a correlation between PPP precision error and the ROTI and deemed to be an exponential fit as shown in figure 2 in *Jacobsen and Dähnn* [2014]. This fits with our findings, as we see increase in ROTI and GNSS error at the same time, but only at the medium bin Figure 4.4 and the strong bin Figure 4.5. In the weak bin we see a small, relative to the other bins, increase in ROTI, but no increase in GNSS error. This can possibly point to that there is needed a ROTI threshold before one can see the increase in GNSS-error or the quality of the bin is not sufficient to see the relationship between GNSS error and ROTI. However the article has used a different method than in this thesis, where they took all ROTI values, not only specific ones related to substorm activity, so it is not a clear comparison. They also used a different year 2012, and since then the CPOS system has integrated data from Galileo into its processing in 2017 (Knut S. Jacobsen, personal communication), so we can expect a higher accuracy from the 2018 data in this thesis. Therefore we can not conclude anything from this, but it shows more research is needed to study this relationship.

c GNSS

In the GNSS part of Figures 4.3, 4.4, 4.5, 4.6, we can see the GNSS-noise plotted on a logarithmic scale. This was to better show that noise varies constantly where the 95th and 5th percentile are almost constantly between the $3 \cdot 10^{-4}$ and $3 \cdot 10^{-3}$ meters on the full data plot and within the bins. In the 95th percentile, we see a spike in the noise level. This is interesting as this is a logarithmic scale, so the increase is quite significant and goes up to 5 cm. This is not the centimeter accuracy we expect from CPOS, and shows a clear disruption of the system. This is for the 95 percentile, which means that at least 5 percent of substorms makes the GNSS-receiver breach the 1 cm threshold. This is most likely an increased ionospheric delay. We can see that one hour until the event occurred, the error remains below $3 \cdot 10^{-3}$ meters and peaks at the same time as the ROTI measures the peak. Therefore we argue that this peak is caused by the ionospheric effect. Furthermore, we see that the weak bin of the GNSS noise in Figure 4.4, has no spike, where as the other bins or all the data plots do. However, the medium bin and strong bin, Figures 4.5 and 4.6 show an increased noise level in the 95th percentile shortly after the event time. This indicates that the events in the weak bin are likely either a false positive or too weak to be disruptive to GNSS receiver. This also can be due to satellite availability as the more satellites the receiver has access to, the better the positioning. It can be the case that there is a scintillation event occurring, but it is localized such that enough satellites signals can pass unaffected through the ionosphere and give a reliable accuracy. It could also be that there is a scintillation event occurred, but is far enough away from Tromsø that it does not affect the receiver, but is measurable for the magnetometer. There is not much literature about the GNSS-accuracy on the CPOS, so we will compare to a different network in Belgia called AGN (Active Geodetic Network) described in the paper *Lejeune et al.* [2012]. Note that the network is in mid-latitude and in the article, they look at the effect of a geomagnetic storm, not substorm. However they see during a geomagnetic storm, that the positioning worsened to over a centimeter during the storm and concluded the inaccuracy to ionospheric disturbances. This is consistent with our findings in this thesis, that the ionosphere has a considerate impact of RTK Networks.

We however need for more research to conclude if this is scintillation event. By looking into scintillation data and looking at the phase scintillation for elevated values *Aquino et al.* [2005], we can determine if the event is caused by scintillation or some other source.

d Comparison of the magnetometer, ROTI and GNSS-error

We compare our results to *Follestad et al.* [2021] as they preformed a similar superposed epoch analysis of the RTK system. Here they have used an algorithm to find times where the algorithm look for GNSS-error over a threshold and compare this ionospheric measurements like ROTI, AE, B_z value of the solar wind and other parameters. Note that they looked at 3 years of data, 2014 to 2016, while in this thesis we look at one year 2018.

They compared three stations shown in Figure 8 in *Follestad et al.* [2021], where Tromsø is one of them, and they have an algorithm to find heightened GNSS-error. They also found a heightened peak in the ROTI and a dip in magnetometers values as in this thesis. This was noticeable in Tromsø, but not in the southern stations Steinkjer and Stavanger. Note that the algorithm they were using to locate events is different from our method, as theirs looks for GNSS errors purely and this can be caused by other phenomena like multipath and other disturbances. However it is interesting to see that by using two different methods for finding events, one through GNSS error and one through magnetometer readings, we get the same type of plots. We can see that the ground magnetometers averaging of the events in the article *Follestad et al.* [2021] do not measure that low of a dip as in this thesis. This could be due to averaging of 3 years, instead getting the median of 1 year as that can lower the dip. Also it could be an effect of the two different methods used to locate the events, as we also see a higher peak in GNSS error in *Follestad et al.* [2021], than in our results. Regardless, since the similarity is still quite big, we can say that ionospheric effect has a large impact on the CPOS network in Tromsø.

They also looked at the performance of the CPOS system in the article *Jacobsen and Andalsvik* [2016], but here they looked at a single Geomagnetic storm, not multiple substorms as done in this thesis. In Figure 11 in the article, they did a binning of different ROTI values to show the average values and they also found a correlation between the GNSS-error and ROTI. They also looked at the Auroral Electrojet Figure 3c, where they presented a total sum of the eastward and westward integrated currents. They found a relationship as in this thesis, but they noted that it is not a clear linear relationship between the two. In this thesis we found the relationship to ROTI is possibly linked to the gradients of the magnetometer value, but further research needs be done in order to confirm this. However we can see that in *Jacobsen and Andalsvik* [2016] and this thesis that there is a correlation between magnetometer, ROTI and GNSS-accuracy. It also interesting to see a higher value of GNSS-error than for lower ROTI. Given that *Jacobsen and Andalsvik* [2016] is a much stronger geomagnetic storm and only one storm, compared to our weaker averaged substorms. This would indicate that although correlated ROTI and GNSS-Error, it seems it depends on other factors as well, and shows it is difficult to assign a certain function to it. The system will see improvements as time passes, as more satellites are available and hardware gets upgraded, as that could explain why we get smaller GNSS-errors in this thesis. We would need a same year analysis to remove the uncertainty from the comparison to further determine what the higher GNSS error in *Jacobsen and Andalsvik* [2016].

For the medium and strong bin, Figures 4.5 and 4.6, we can see that the spike of the GNSS noise is right underneath the ROTI spike. We also see that GNSS-error is not constant, although the ROTI remains constantly high. If this is a scintillation event, this can be explained to be open areas where the ionospheric plasma is not disturbed. Therefore some satellites might be able to get through without passing through density fluctuations. There can also be a varying amount of available satellites through the event, so this will also have an impact as more satellites will improve the positioning accuracy. These peaks that we see in the ROTI and GNSS-error are likely due to ionospheric effect as when new plasma is introduced i.e. through particle precipitation *Martin and Aarons* [1977] or polar cap patches *Jin et al.* [2016]. These introductions to plasma can cause scintillation to occur. It could also be associated with the field aligned currents causing scintillation *Fæhn Follestad et al.* [2020] *Clausen et al.* [2016]. As the Kelvin Helmholtz and Gradient Drift instabilities causes density fluctuations *Hargreaves* [1992], *Basu et al.* [1990], this would give the signal a varying amount of ionospheric delay. This would provide a GNSS error consistent with our data.

We have shown that there is correlation between the GNSS accuracy, ROTI and the strength of the Auroral Electrojet current at the filtered SuperMAG events taken from *Newell and Gjerloev* [2011], and the GNSS error is considerable for the strongest event found in this thesis. We can not say for certain that this is due to phase scintillation without looking at phase scintillation index data, but we argue that it is most likely so. However this provides a good way to study events from a statistical standpoint and how they affect positioning services.

Chapter 6

Conclusion

6.1 Summary

This thesis presents a years worth of data, where we have filtered the SuperMAG event list from *Newell and Gjerloev* [2011] to identify substorms at Tromsø in northern Norway. With superposed epoch analysis, we analyzed a 4 hour window at these event times to look at magnetometer data, ROTI data and Network RTK GNSS-receiver accuracy. In addition, we have sorted the events by strength of the substorms by magnetometer impact. We divided them into three bins with approximately the same amount of substorms in each, where the weak bin has the weakest substorms, medium bin has moderate substorms and the strong bin has the strongest substorms.

We managed to find relevant substorm times using the substorm event list with filtering as the magnetometer median value decreased at the listed times.

This indicates that the Auroral Electrojet current is increasing in strength at the listed times. However, we also see a few non-relevant events in the list. Hence the filtering we performed in this thesis is not sufficient to remove all non-relevant events.

During the event times we see a clear correlation between a decreasing value of the magnetometer, an increase of ROTI values and decrease of the GNSS-receiver accuracy. The GNSS noise increased to 5cm in the 95 % percentile which goes over the 1 cm accuracy threshold that the CPOS system is supposed to deliver. We attribute the increased GNSS-error to an ionospheric effect as seen in other theses such as *Jacobsen and Andalsvik* [2016] and *Follestad et al.* [2021], but can not conclude on this being scintillation as this needs to be verified with phase measurements.

We conclude that the filtered SuperMAG event times are a sufficient way to get relevant substorms for Northern Norway and showed that the strongest substorms made an impact on the CPOS system with an inaccuracy up to the decimeter level.

6.2 Outlook

Although the list and filtering proved successful, it has room for improvement. It would be very interesting to see if one could used the SuperMAG algorithm specified in *Newell and Gjerloev* [2011] on a singular magnetometer, i.e the Tromsø magnetometer used in this report. This could provide a list more specific for Tromsø and maybe have higher certainty. There is also another algorithm available to gather lists of substorms i.e. *Ohtani and Gjerloev* [2020] that could also be used on a specific magnetometer station. The list generated with this algorithm is not intended for statistical analysis, but produces a substorm list that is of high certainty and could have less false negatives.

The data used in this thesis was taken from a year with solar minimum, so we suggest to see if the analysis could be done over multiple years including a solar maximum as to increase the sample size. With an increased sample size, one can also investigate seasonal variations and the time of day substorms occur.

a Machine learning utilities

One use of substorm lists is in machine learning, where algorithms can learn how to identify and recognize substorms.

As shown in this thesis, one can use the SuperMAG event list to make a dataset of relevant events for a specific location and use the three data sources as features to create a machine learning model for both detecting and predicting events. We suggest using a machine learning method from *Linty et al.* [2019] or *McGranaghan et al.* [2018] to train on the data from this thesis. The detection of the events is valuable input to the user of the CPOS system, as it provides input on validity of the readings. Therefore, this can lead to higher reliability of the positioning. There are still challenges, *Camporeale* [2019] to further develop these methods, but there is a lot of potential in this field.

We recommend looking into prediction or forecasting of these events *Moen et al.* [2013]. This would be like a weather forecast, but it would predict a geomagnetic storm activity instead. This would be very valuable as an event could make the GNSS-receiver inaccurate as seen in this thesis or even predict a more severe geomagnetic storm that can be more detrimental. Currently there is work being done on a forecasting system for Norway *Fabbro et al.* [2021] through the NMA (Norwegian Mapping Authority), where they use solar wind data which is measured an hour away from the Earth to compute a forecasting on the reliability of their receivers.

It is still in its prototype stage, but shows promise. There is also work being done at ESA (European Space Agency) where they are developing machine learning algorithms to detect scintillation events. Some of this work will be represented at the INC (International Navigation Conference) and ENC (European Navigation Conference) *Calabrese* [2021]

Bibliography

Aarons, J., Global positioning system phase fluctuations at auroral latitudes, *Journal of Geophysical Research: Space Physics*, *102*(A8), 17,219–17,231, doi:https://doi.org/10.1029/97JA01118, 1997.

Aquino, M., T. Moore, A. Dodson, S. Waugh, J. Souter, and F. S. Rodrigues, Implications of ionospheric scintillation for gnss users in northern europe, *Journal of Navigation*, *58*(2), 241–256, doi:10.1017/S0373463305003218, 2005.

Basu, S., S. Basu, E. MacKenzie, W. R. Coley, J. R. Sharber, and W. R. Hoegy, Plasma structuring by the gradient drift instability at high latitudes and comparison with velocity shear driven processes, *Journal of Geophysical Research: Space Physics*, *95*(A6), 7799–7818, doi:https://doi.org/10.1029/JA095iA06p07799, 1990.

Basu, S., K. Groves, J. Quinn, and P. Doherty, A comparison of tec fluctuations and scintillations at ascension island, *Journal of Atmospheric and Solar-Terrestrial Physics*, *61*(16), 1219–1226, 1999.

Basu, S., K. Groves, S. Basu, and P. Sultan, Specification and forecasting of scintillations in communication/navigation links: current status and future plans, *Journal of Atmospheric and Solar-Terrestrial Physics*, *64*(16), 1745–1754, doi:https://doi.org/10.1016/S1364-6826(02)00124-4, space Weather Effects on Technological Systems, 2002.

Buonsanto, M. J., Ionospheric storms—a review, *Space Science Reviews*, *88*(3), 563–601, 1999.

Burston, R., I. Astin, C. Mitchell, L. Alfonsi, T. Pedersen, and S. Skone, Turbulent times in the northern polar ionosphere?, *Journal of Geophysical Research: Space Physics*, *115*(A4), doi:https://doi.org/10.1029/2009JA014813, 2010.

Calabrese, A., Aimgnss – a tool and framework for investigating the application of machine learning techniques to gnss anomaly detection, in *Proc. of the 6th Nordic Conf. on Human-Computer Interaction*, ENC and INC, Netherlands, 2021.

Campbell, W. H., *Introduction to geomagnetic fields*, Cambridge University Press, 2003.

Camporeale, E., The challenge of machine learning in space weather: Nowcasting and forecasting, *Space Weather*, *17*(8), 1166–1207, doi:https://doi.org/10.1029/2018SW002061, 2019.

Cander, L. R., and S. J. Mihajlovic, Forecasting ionospheric structure during the great geomagnetic storms, *Journal of Geophysical Research: Space Physics*, *103*(A1), 391–398, doi:https://doi.org/10.1029/97JA02418, 1998.

Carlson, H. C., Sharpening our thinking about polar cap ionospheric patch morphology, research, and mitigation techniques, *Radio Science*, *47*(4), doi:https://doi.org/10.1029/2011RS004946, 2012.

Clausen, L. B. N., J. B. H. Baker, J. M. Ruohoniemi, S. E. Milan, J. C. Coxon, S. Wing, S. Ohtani, and B. J. Anderson, Temporal and spatial dynamics of the regions 1 and 2 birkeland currents during substorms, *Journal of Geophysical Research: Space Physics*, *118*(6), 3007–3016, doi:https://doi.org/10.1002/jgra.50288, 2013.

Clausen, L. B. N., J. I. Moen, K. Hosokawa, and J. M. Holmes, Gps scintillations in the high latitudes during periods of dayside and nightside reconnection, *Journal of Geophysical Research: Space Physics*, *121*(4), 3293–3309, doi:https://doi.org/10.1002/2015JA022199, 2016.

Cowley, S., and M. Lockwood, Excitation and decay of solar wind-driven flows in the magnetosphere-ionosphere system, in *Annales geophysicae*, vol. 10, pp. 103–115, 1992.

C.T. Russel, J., and R. Strangeway, *Space physics an introduction*, Cambridge University Press, Cambridge, UK, 2016.

Davis, T. N., and M. Sugiura, Auroral electrojet activity index ae and its universal time variations, *Journal of Geophysical Research (1896-1977)*, *71*(3), 785–801, doi:https://doi.org/10.1029/JZ071i003p00785, 1966a.

Davis, T. N., and M. Sugiura, Auroral electrojet activity index ae and its universal time variations, *Journal of Geophysical Research (1896-1977)*, *71*(3), 785–801, doi:https://doi.org/10.1029/JZ071i003p00785, 1966b.

Dungey, J. W., Interplanetary magnetic field and the auroral zones, *Physical review letters*, *6, number2*, 1961.

Eastwood, J. P., The science of space weather, *Philosophical Transactions of the Royal Society A: Mathematical, Physical and Engineering Sciences*, *366*(1884), 4489–4500, 2008.

ESA, Gnss measurements modelling, *GNSS Measurements Modelling - Navipedia*.

ESA, C. R., Earth's magnetosphere, 2007.

Fabbro, V., K. S. Jacobsen, Y. L. Andalsvik, and S. Rougerie, Gnss positioning error forecasting in the arctic: Roti and precise point positioning error forecasting from solar wind measurements, *Journal of Space Weather and Space Climate*, *11*, 43, 2021.

Follestad, A. F., L. B. N. Clausen, J. I. Moen, and K. S. Jacobsen, Latitudinal, diurnal, and seasonal variations in the accuracy of an rtk positioning system and its relationship with ionospheric irregularities, *Space Weather*, *19*(6), e2020SW002,625, doi:https://doi.org/10.1029/2020SW002625, e2020SW002625 2020SW002625, 2021.

Forsyth, C., I. J. Rae, J. C. Coxon, M. P. Freeman, C. M. Jackman, J. Gjerloev, and A. N. Fazakerley, A new technique for determining substorm onsets and phases from indices of the electrojet (sophie), *Journal of Geophysical Research: Space Physics*, *120*(12), 10,592–10,606, doi:https://doi.org/10.1002/2015JA021343, 2015.

Frank, L. A., and J. D. Craven, Imaging results from dynamics explorer 1, *Reviews of Geophysics*, *26*(2), 249–283, doi:https://doi.org/10.1029/RG026i002p00249, 1988.

Fremouw, E., R. Leadabrand, R. Livingston, M. Cousins, C. Rino, B. Fair, and R. Long, Early results from the dna wideband satellite experiment—complex-signal scintillation, *Radio Science*, *13*(1), 167–187, 1978.

Fæhn Follestad, A., K. Herlingshaw, H. Ghadjari, D. J. Knudsen, K. A. McWilliams, J. I. Moen, A. Spicher, J. Wu, and K. Oksavik, Dayside field-aligned current impacts on ionospheric irregularities, *Geophysical Research Letters*, *47*(11), e2019GL086,722, doi:https://doi.org/10.1029/2019GL086722, e2019GL086722 10.1029/2019GL086722, 2020.

Germany, G. A., G. K. Parks, M. Brittnacher, J. Cumnock, D. Lummerzheim, J. F. Spann, L. Chen, P. G. Richards, and F. J. Rich, Remote determination of auroral energy characteristics during substorm activity, *Geophysical Research Letters*, *24*(8), 995–998, doi:https://doi.org/10.1029/97GL00864, 1997.

Gjerloev, J., R. Hoffman, M. Friel, L. Frank, and J. Sigwarth, Substorm behavior of the auroral electrojet indices, in *Annales Geophysicae*, vol. 22, pp. 2135–2149, Copernicus GmbH, 2004.

Gjerloev, J. W., The supermag data processing technique, *Journal of Geophysical Research: Space Physics*, *117*(A9), doi:https://doi.org/10.1029/2012JA017683, 2012.

Gonzalez, W., J.-A. Joselyn, Y. Kamide, H. W. Kroehl, G. Rostoker, B. Tsurutani, and V. Vasyliunas, What is a geomagnetic storm?, *Journal of Geophysical Research: Space Physics*, *99*(A4), 5771–5792, 1994.

Gonzalez, W., E. Echer, A. C. de Gonzalez, B. Tsurutani, and G. Lakhina, Extreme geomagnetic storms, recent gleissberg cycles and space era-superintense storms, *Journal of Atmospheric and Solar-Terrestrial Physics*, *73*(11-12), 1447–1453, 2011.

Hargreaves, J. K., *The solar-terrestrial environment: an introduction to geospace-the science of the terrestrial upper atmosphere, ionosphere, and magnetosphere*, Cambridge university press, 1992.

Hernández-Pajares, M., J. M. Juan, J. Sanz, À. Aragón-Àngel, A. García-Rigo, D. Salazar, and M. Escudero, The ionosphere: effects, gps modeling and the benefits for space geodetic techniques, *Journal of Geodesy*, *85*(12), 887–907, 2011.

Hey, J., S. Parsons, and J. Phillips, Fluctuations in cosmic radiation at radio-frequencies, *Nature*, *158*(4007), 234–234, 1946.

Hofmann-Wellenhof, E. W., B. H. Lichtenegger, *GNSS - Global Navigation Satellite Systems: GPS, GLONASS, Galileo* & *more*, SpringerWienNewYork, 2008.

Hundhausen, A., Coronal mass ejections, in *The Many Faces of the Sun*, pp. 143–200, Springer, 1999.

Irsigler, M., G. W. Hein, and B. Eissfeller, Multipath performance analysis for future gnss signals, in *Proceedings of the 2004 National Technical Meeting of The Institute of Navigation*, pp. 225–238, 2004.

Jacobsen, K. S., and Y. L. Andalsvik, Overview of the 2015 st. patrick's day storm and its consequences for rtk and ppp positioning in norway, *Journal of Space Weather and Space Climate*, *6*, A9, 2016.

Jacobsen, K. S., and M. Dähnn, Statistics of ionospheric disturbances and their correlation with gnss positioning errors at high latitudes, *Journal of Space Weather and Space Climate*, *4*, A27, 2014.

Jakowski, N., Y. Béniguel, G. De Franceschi, M. H. Pajares, K. S. Jacobsen, I. Stanislawska, L. Tomasik, R. Warnant, and G. Wautelet, Monitoring, tracking and forecasting ionospheric perturbations using gnss techniques, *Journal of Space Weather and Space Climate*, *2*, A22, 2012.

Jin, Y., J. I. Moen, and W. J. Miloch, Gps scintillation effects associated with polar cap patches and substorm auroral activity: Direct comparison, *Journal of Space Weather and Space Climate*, *4*, A23, 2014.

Jin, Y., J. I. Moen, and W. J. Miloch, On the collocation of the cusp aurora and the gps phase scintillation: A statistical study, *Journal of Geophysical Research: Space Physics*, *120*(10), 9176–9191, 2015.

Jin, Y., J. I. Moen, W. J. Miloch, L. B. N. Clausen, and K. Oksavik, Statistical study of the gnss phase scintillation associated with two types of auroral blobs, *Journal of Geophysical Research: Space Physics*, *121*(5), 4679–4697, doi: https://doi.org/10.1002/2016JA022613, 2016.

Kamide, Y., and S.-I. Akasofu, The auroral electrojet and field-aligned current, *Planetary and Space Science*, *24*(3), 203–213, doi:https://doi.org/10.1016/0032-0633(76)90017-9, 1976.

Kersley, L., C. D. Russell, and D. L. Rice, Phase scintillation and irregularities in the northern polar ionosphere, *Radio Science*, *30*(3), 619–629, doi:10.1029/94RS03175, 1995.

Kintner, P. M., B. M. Ledvina, and E. R. de Paula, Gps and ionospheric scintillations, *Space Weather*, *5*(9), doi:https://doi.org/10.1029/2006SW000260, 2007.

Kouba, J., and P. Héroux, Precise point positioning using igs orbit and clock products, *GPS solutions*, *5*(2), 12–28, 2001.

K.S. Jacobsen, S. S., Observed effects of a geomagnetic storm on an rtk positioning network at high latitudes, *Space Weeather Space Clim*, *2, A13*, 2012.

Lejeune, S., G. Wautelet, and R. Warnant, Ionospheric effects on relative positioning within a dense gps network, *GPS solutions*, *16*(1), 105–116, 2012.

Linty, N., A. Farasin, A. Favenza, and F. Dovis, Detection of gnss ionospheric scintillations based on machine learning decision tree, *IEEE Transactions on Aerospace and Electronic Systems*, *55*(1), 303–317, doi:10.1109/TAES.2018.2850385, 2019.

Martin, E., and J. Aarons, F layer scintillations and the aurora, *Journal of Geophysical Research (1896-1977)*, *82*(19), 2717–2722, doi:https://doi.org/10.1029/JA082i019p02717, 1977.

McGranaghan, R. M., A. J. Mannucci, B. Wilson, C. A. Mattmann, and R. Chadwick, New capabilities for prediction of high-latitude ionospheric scintillation: A novel approach with machine learning, *Space Weather*, *16*(11), 1817–1846, doi:https://doi.org/10.1029/2018SW002018, 2018.

McPherron, R. L., C. T. Russell, and M. P. Aubry, Satellite studies of magnetospheric substorms on august 15, 1968: 9. phenomenological model for substorms, *Journal of Geophysical Research (1896-1977)*, *78*(16), 3131–3149, doi:https://doi.org/10.1029/JA078i016p03131, 1973.

Moen, J., K. Oksavik, L. Alfonsi, Y. Daabakk, V. Romano, and L. Spogli, Space weather challenges of the polar cap ionosphere, *Journal of Space Weather and Space Climate*, *3*, A02, 2013.

National_Oceanic, and Atmospheric_Administration, Solar cycle progression, online article https://www.swpc.noaa.gov/products/solar-cycle-progression, 2021.

Newell, P. T., and J. W. Gjerloev, Evaluation of supermag auroral electrojet indices as indicators of substorms and auroral power, *Journal of Geophysical Research: Space Physics*, *116*(A12), doi:https://doi.org/10.1029/2011JA016779, 2011.

Ohma, A., J. P. Reistad, and S. M. Hatch, Modulation of magnetospheric substorm frequency: Dipole tilt and imf by effects, *Journal of Geophysical Research: Space Physics*, *126*(3), e2020JA028,856, doi:https://doi.org/10.1029/2020JA028856, e2020JA028856 2020JA028856, 2021.

Ohtani, S., and J. W. Gjerloev, Is the substorm current wedge an ensemble of wedgelets?: Revisit to midlatitude positive bays, *Journal of Geophysical Research: Space Physics*, *125*(9), e2020JA027,902, doi:https://doi.org/10.1029/2020JA027902, e2020JA027902 2020JA027902, 2020.

Owens, M. J., and R. J. Forsyth, The heliospheric magnetic field, *Living Reviews in Solar Physics*, *10*(1), 1–52, 2013.

Paschmann, G., et al., Plasma acceleration at the earth's magnetopause: Evidence for reconnection, *Nature*, *282*, doi:10.1038/282243a0, 1979.

Pécseli, H. L., *Waves and oscillations in plasmas*, CRC Press Boca Raton, 2013a.

Pécseli, H. L., *Waves and oscillations in plasmas*, CRC Press Boca Raton, 2013b.

Prölss, G., *Physics of the Earth's space environment: an introduction*, Springer Science & Business Media, 2012.

Rizos, C., et al., Network rtk research and implementation-a geodetic perspective, *Positioning*, *1*(02), 2009.

Rostoker, G., S.-I. Akasofu, J. Foster, R. Greenwald, A. Lui, Y. Kamide, K. Kawasaki, and R. McPherron, Magnetospheric substorms - definition and signatures, *Journal of Geophysical Research*, *85*, 1663–1668, doi:10.1029/JA085iA04p01663, 1980.

Saastamoinen, J., *Atmospheric Correction for the Troposphere and Stratosphere in Radio Ranging Satellites*, pp. 247–251, American Geophysical Union (AGU), doi:https://doi.org/10.1029/GM015p0247, 1972.

Singh, A., D. Siingh, and R. Singh, Space weather: physics, effects and predictability, *Surveys in geophysics*, *31*(6), 581–638, 2010.

Siscoe, G., and T. Huang, Polar cap inflation and deflation, *Journal of Geophysical Research: Space Physics*, *90*(A1), 543–547, 1985.

Skone, S., M. Feng, R. Tiwari, and A. Coster, Characterizing ionospheric irregularities for auroral scintillations, in *Proceedings of the 22nd International Technical Meeting of the Satellite Division of The Institute of Navigation (ION GNSS 2009)*, pp. 2551–2558, 2009.

Spicher, A., K. Deshpande, Y. Jin, K. Oksavik, M. D. Zettergren, L. B. N. Clausen, J. I. Moen, M. R. Hairston, and L. Baddeley, On the production of ionospheric irregularities via kelvin-helmholtz instability associated with cusp flow channels, *Journal of Geophysical Research: Space Physics*, *125*(6), e2019JA027,734, doi:https://doi.org/10.1029/2019JA027734, e2019JA027734 10.1029/2019JA027734, 2020.

Tiwari, R., H. Strangeways, S. Tiwari, and A. Ahmed, Investigation of ionospheric irregularities and scintillation using tec at high latitude, *Advances in Space Research*, *52*(6), 1111–1124, 2013.

Van Dierendonck, A., J. Klobuchar, and Q. Hua, Ionospheric scintillation monitoring using commercial single frequency c/a code receivers, in *proceedings of ION GPS*, vol. 93, pp. 1333–1342, Citeseer, 1993.

Wang, H., H. Lühr, and S. Y. Ma, Solar zenith angle and merging electric field control of field-aligned currents: A statistical study of the southern hemisphere, *Journal of Geophysical Research: Space Physics*, *110*(A3), doi:https://doi.org/10.1029/2004JA010530, 2005.

Y. Jin, J. M., W. Miloch, and L. Clausen, Solar cycle and seasonal variations of the gps phase scintillation at high latitudes, *J. Space Weather Space Clim, 8, A48*, 2018.

Yamada, M., R. Kulsrud, and H. Ji, Magnetic reconnection, *Reviews of Modern Physics*, *82*(1), 603, 2010.

Yeh, K. C., and C.-H. Liu, Radio wave scintillations in the ionosphere, *Proceedings of the IEEE*, *70*(4), 324–360, doi:10.1109/PROC.1982.12313, 1982.

Zumberge, J. F., M. B. Heflin, D. C. Jefferson, M. M. Watkins, and F. H. Webb, Precise point positioning for the efficient and robust analysis of gps data from large networks, *Journal of Geophysical Research: Solid Earth*, *102*(B3), 5005–5017, doi:https://doi.org/10.1029/96JB03860, 1997.

Appendix A

Parameters for the instruments

magnetometer

In this thesis we selected the Tromsø magnetometer which is located 69.66 degrees north and 18.94 degrees east in Northern Norway.

ROTI data

The raw ROTI is from the NMA and cannot be shared openly.

GNSS-receiver info

The receiver is from Topcon Positioning Systems, where the type name is:
Geodetic Quality Multi-frequency Receiver.
The link to the website is:
`https://www.topconpositioning.com/gnss-and-network-solutions/gnss-antennas/cr-g5`
The CPOS Monitor in Tromsø (MTRM) uses these instruments:
Receiver: TPS NET-G5 (25.12.2017 - now)
Antenna: TPSCR.G5 (25.12.2017 - now)
For more info, the link to the data sheet of the CPOS monitor is:
`https://www.topconpositioning.com/sites/default/files/product_files/net-g5_datasheet_7010-2145_revf_ltr_en_us_lores.pdf`

Appendix B

Filtering parameters

Original number	filtering time and latitude	removing duplicates	missing GNSS data
1256	319	276	197

Table B.1: A table over each of the filtering criteria showing how much they reduce the original number of event list, step by step.